3D Thermal-Electrochemical Lithium-Ion Battery Computational Modeling

by

Rachel Ellen Gerver, BS

Thesis

Presented to the Faculty of the Graduate School of
The University of Texas at Austin
in Partial Fulfillment
of the Requirements
for the Degree of

Master of Science in Engineering

The University of Texas at Austin
August 2009

3D Thermal-Electrochemical Lithium-Ion Battery Computational Modeling

Approved by
Supervising Committee:

Jeremy Meyers

Ofodike Ezekoye

Acknowledgements

I would like to especially thank my advisor Dr. Jeremy Meyers for his encouragement and research guidance throughout my Masters program at UT Austin. He was an extremely positive and supportive advisor both in research and other areas.

A number of other people also contributed to this work. Dr. Karen Thomas-Alyea, a research scientist and battery expert at A123 Systems, provided valuable guidance in shaping the direction of this computational modeling research by giving us perspective on industry needs and in-depth knowledge of computational modeling approaches to electrochemical systems. Michael Nawrocki, an undergraduate research assistant in the lab, was helpful in pulling together some of the material property data in the model, for which tracking down information was no easy feat. I also appreciated Dr. Ofodike Ezekoye's guidance on the heat transfer components of the model.

The other members of the Meyers Research Group were incredibly supportive and a pleasure to work with. Katie Harrison, in particular, was very helpful in providing knowledge of lithium iron phosphate batteries and expertise in computational modeling when I ran into research issues.

Lastly, I would like to thank the National Science Foundation Graduate Fellowship Program, A123 Systems, and the University of Texas at Austin College of Engineering Thrust 2000 Scholarship program for funding support during my graduate studies.

August 2009

Abstract

3D Thermal-Electrochemical Lithium-Ion Battery Computational Modeling

Rachel Ellen Gerver, M.S.E.
The University of Texas at Austin, 2009
Supervisor: Jeremy P Meyers

The thesis presents a modeling framework for simulating three dimensional effects in lithium-ion batteries. This is particularly important for understanding the performance of large scale batteries used under high power conditions such as in hybrid electric vehicle applications. While 1D approximations may be sufficient for the smaller scale batteries used in cell phones and laptops, they are severely limited when scaled up to larger batteries, where significant 3D gradients can develop in concentration, current, temperature, and voltage. Understanding these 3D effects is critical for designing lithium-ion batteries for improved safety and long term durability, as well as for conducting effective design optimization studies. The model couples an electrochemical battery model with a thermal model to understand how thermal effects will influence electrochemical behavior and to determine temperature distributions throughout the battery. Several modeling example results are presented including thermal influences on current distribution, design optimization of current collector thickness and current collector tab placement, and investigation of lithium plating risk in three dimensions.

Table of Contents

Chapter 1: Background

1.1 INTRODUCTION

Lithium ion batteries, already common in cell phones, laptops, and other portable electronics devices, are viewed as promising candidates for hybrid electric and electric vehicle applications. This is primarily due to the high energy and power density as compared to other battery chemistries such as NiMH and lead acid, which have traditionally been used in automotive applications. Understanding how lithium ion batteries perform when scaled up to the large size needed for vehicle propulsion applications is important for the design and control of batteries for improved performance, safety, and long term durability. While Li-ion batteries that only last a few years may be sufficient for other applications, batteries which can last the life of a vehicle, typically considered ~10 years, are critical for the development of cost-effective electrified vehicles that can compete in the marketplace.

Some factors influencing battery durability and safety include state of charge operating range, lithium plating on the graphite anode, and battery temperature. Different lithium ion battery chemistries have different ranges of charge and discharge under which they are stable. Operating outside of this range can lead to chemical instabilities in the electrode material that can cause battery degradation over time or even immediate safety issues due to unwanted side reactions.

Lithium plating occurs when the potential of the anode, measured as ($\Phi_1 - \Phi_2$) the solid potential minus the solution potential, drops below the lithium reference potential.

When this occurs, lithium ions will plate out as solid lithium on the surface of the anode rather than inserting into the electrode material to form Li_xC_6. This leads to a loss of available lithium to store energy in the battery and a blocking of access to parts of the electrode; excessive plating can lead to dendritic growth across the separator which short-circuits the battery and renders it unsafe.

Batteries have an optimal temperature range over which peak performance can be obtained. Extreme temperatures on either end can lead to battery damage and/or loss of performance. High temperatures can drive unwanted side reactions eventually leading to thermal runaway or accelerated degradation.

These three factors: state of charge, temperature, and potential can vary locally within a battery cell. Gradients are particularly significant with large scale batteries operating under high power conditions as is the case in hybrid electric vehicle applications. Understanding the 3D distribution of potential, current, reaction rate, temperature, heat generation, state of charge, and other properties is important in optimizing the design and control of lithium ion batteries for larger scale applications.

1.2 BATTERY STRUCTURE

A battery consists of five basic layers as shown below: an anode and cathode between which lithium ions are shuttled, a separator that prevents electron flow between the electrodes, and a current collector on the outside of each electrode. Electrons enter and leave the current collectors via current collector tabs, which connect the battery to the external circuit that contains the load to be powered or the source for battery charging.

As will be described in the results, the location and size of these tabs can have a significant impact on overall battery performance.

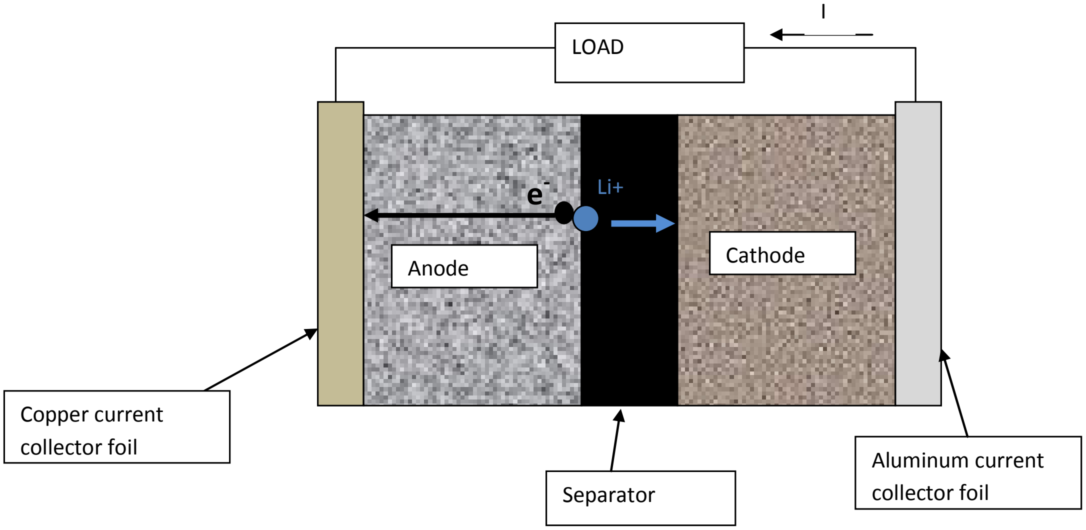

Figure 1: Diagram of a lithium-ion battery

During discharge, lithium ions are shuttled from the anode to the cathode and during charging the reverse process occurs. This is often referred to as a "rocking chair" mechanism. As will be described in more detail in section 1.4, an electrochemical reaction takes place at the electrode/electrolyte interface. In the anodic direction, a lithium ion (Li^+) enters the electrolyte and an electron flows through the electrode to the external circuit. In the cathodic direction, Li^+ enters the electrode from the electrolyte and is joined with an electron from the external circuit. The separator forces all the electrons to flow outside the battery, forcing the current through the external circuit that will include the load that the battery is powering.

The electrodes are generally composed of porous materials, which allow for much higher interfacial surface areas between the electrode and electrolyte and consequently allow much higher reaction rates and greater electrode utilization than would be possible with a solid material.

A variety of materials have been used as the cathode for lithium ion batteries. Traditionally, transition metal oxides, including Li_xCoO2, Li_xMnO_2 and Li_xNiO_2 as well as combinations of those materials, have been used. More recently $LiFePO_4$ has been commercialized as a promising electrode material and is the focus of the simulations in this thesis. While all of the example simulations utilize a $LiC_6/LiPF_6/LiFePO_4$ cell, the model is designed to simulate any combination of anode, cathode, and electrolyte provided that the material property data is available for the components.

1.3 PRIOR 3D BATTERY MODELING WORK

Prior studies have used various methodologies to determine temperature and/or current distributions in lithium ion and other battery chemistries. In some models, heat generation is treated as uniform throughout the core region of the system [1] [2] [3] [4], or include current distribution between cells in a stack, but neglect current distribution and corresponding temperature effects along the length and height of a single cell [5] [6]. Other models allow for local variations in heat generation in 3D, but require pre-specification of local current and voltage from either experimental data or other simulations [7] [8] [9], which limits predictive capabilities.

Several papers have tackled the challenge of determining current distribution in a battery cell. Bernardi et al present a 2D isothermal electrochemical model for lead acid batteries, in which the electrochemical equations are fully solved in two dimensions demonstrating the higher current distributions near the current collector tabs [10]. Tang et al. use COMSOL to solve current and potential distributions along the length of the battery and demonstrate how extending the negative electrode reduces preferential lithium plating at the edges [11]. The model is treated as isothermal with linear kinetics and spatially uniform potential in solid film electrodes. Kwon et al use FEM to study potential and current distribution in lithium-polymer batteries and determine current-voltage profiles using fitting parameters to experimental data as a function of depth of discharge [12]. Verbrugge developed a thermal-electrochemical battery model to simulate 3D current and temperature distributions in a stack that is most accurate under low power conditions as concentration gradients are neglected and the current-potential relationship is treated as linear [13]. Baker and Verbrugge also present an analytical solution using perturbation analysis for temperature and current distributions in thin film batteries valid for short times after the start of charge or discharge from a uniform battery state [14].

Other researchers have examined current distributions in spirally wound batteries including Reimers [15] and Harb and LaFollette [16]. Reimers treats stack impedance as a constant value that does not vary with time or space and then solves for current distribution by treating the spiral cell as an unwound battery with current distribution determined by the resistances of the current collector foils and impedance of the cell. He also proposes a method for incorporating stack impedance values that vary with local SOC. Smith and Kim have presented some work simulating temperature and current distributions in 3D where potential drop is neglected along the length of the current collector, but temperature effects on current distributions and electrochemical performance are captured [17]. Harb and LaFollette combine a 1D porous electrode theory electrochemical model with a 2D resistor network to determine current distribution in a spirally wound lead acid cell, but use a different methodology for determining current distribution than presented in this paper [16]. Notably the work of Harb and Lafollete includes the impact of temperature on electrochemical behavior allowing for analysis of the thermal effects on current distributions. Recently their work has been expanded to spirally wound lithium ion batteries [18]. In their methodology, a guess is made for the overall tab potential and the system solved to see if the sum of the local current densities equals the total specified current distribution. If not, a new guess is made for the tab potential. The solution methods for determining current distribution presented in this thesis allow for greater flexibility in applying highly variable current, voltage, or power profiles as might be seen in hybrid vehicle operation.

Another approach taken by some researchers is to use a finite element package to simulate the battery, specifying resistance for each element and calculating the current distribution and resistive heating. Initially done assuming constant resistance by Bharathan et al. [19], this work was expanded by Inui et al to include variable resistance that varies with local SOC and temperature based on experimental data [20]. In Inui's work the core of the battery is treated as homogeneous for the electrochemical reaction, but the anisotropy in thermal conductivity is considered.

Prior work has demonstrated the importance of including the impact of temperature on the electrochemical behavior in accurately simulating battery performance [21][22]. As will be shown in this thesis, neglecting thermal effects can also lead to large inaccuracies in predicting current distribution in a battery cell. Understanding this thermal-electrochemical coupling has implications for understanding safe operating conditions as well as optimizing cooling system design.

The model described in this thesis was developed to better capture the performance of batteries used in large scale, high power applications such as hybrid electric vehicles where significant 3D current and temperature gradients can develop that will influence overall battery performance, safety, and long term durability. A framework is presented for simulating transient battery response on charge and discharge in three dimensions with a coupled thermal-electrochemical battery model.

1.4 ELECTROCHEMICAL MODEL

The electrochemical component of the model is based on porous-electrode theory and the lithium-ion battery modeling work from the Newman group at UC Berkeley [23]. This system of equations is converted to a finite difference matrix formulation and solved iteratively using the Newton-Raphson method in MATLAB.

As will be discussed in Chapter 2, the overall 3D thermal-electrochemical model is composed of a grid of 1D electrochemical models coupled to a thermal model and a 2D resistor network to determine current and temperature distributions in three-dimensions. Figure 2 shows a schematic of the overall model structure, including the grid of 1D electrochemical models that are discussed in this section.

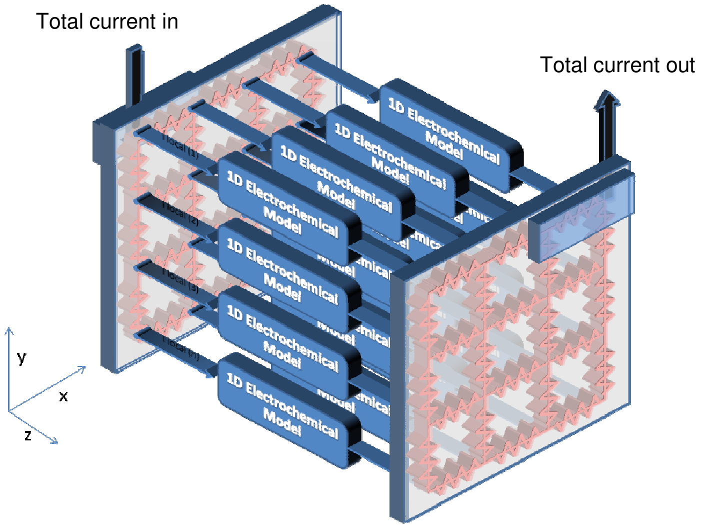

Figure 2: Schematic of overall model structure. Current collector foils are treated as a 2D network of resistors and the electrochemical cell is made up of a grid of 1D electrochemical models. The current enters and leaves the battery through the current collector tabs specified at specific nodes on the battery.

1.4.1 Porous Electrode Theory

The 1D electrochemical portion of this model is based on the lithium ion porous electrode theory dualfoil model developed by Doyle, Fuller and Newman [23]. The exact formulations of the equations used in this model are from the chapter "Mathematical Modeling of Lithium Batteries" by Thomas, Newman and Darling [24].

With porous-electrode theory, rather than specifying the detailed 3D structure at all points, the solid and solution phases are volume averaged and parameters for each of these phases are specified at all points within a control volume. The different solid and solution phases in the electrode are essentially superposed so that they coexist at every point in the electrode. A control volume is chosen that is large with respect to the pores, but small with respect to the overall volume of the electrode. The nature of battery electrodes sometimes makes it impossible to fully justify the use of these approximations, as the size of individual particles and pores can be of the same order as the thickness of the electrodes, but the simplification of model construction and general agreement with experimentally obtained results justifies the loss of precision.

The material properties are specified to account for the porosity as the multiple phases will lead to a longer path length traveled by lithium ions and electrons in the battery. This tortuousity is accounted for by applying Bruggemann's exponent to the conductivity and diffusion coefficients, taking the form:

$$D = D_{bulk}\varepsilon^{B} \qquad [1.1]$$

Where D_{bulk} is the diffusion coefficient in the bulk solution, ε is the porosity, or volume fraction of electrolyte, and B is the Bruggeman exponent which can range in value depending on the particle size and shape distribution. For the purposes of this simulation it is taken to be 2.8 based on the work of Patel *et al* [25] with battery electrode materials.

Because the two phases are superposed, two additional parameters, the interfacial area between the two phases per unit volume of electrode, *a*, and the volume fraction of each phase, *ε,* must be specified. This interfacial area per unit volume is mathematically calculated by treating the solid electrode material as a collection of uniform spheres where:

$$a = N_p(4\pi r^2) \qquad [1.2]$$

and the volume fraction of the solid phase, ε_{s}, is given by:

$$\varepsilon_s = N_p\left(\frac{4}{3}\pi r^3\right) \qquad [1.3]$$

The interfacial area (*a*) is equal to the surface area of each sphere times the number of spheres per unit volume (N_p) and the fraction of the volume occupied by solid material (ε_s) is equal to the volume per sphere times the number of spheres per unit volume (N_p). By combining these equations, N_p can be eliminated and the interfacial area solved for using the known quantities of fraction solid material and particle radius to yield the equation:

$$a = \frac{3\varepsilon_s}{r} \qquad [1.4]$$

1.4.2 Electrochemical Equations

The 1D electrochemical component of the model consists of a set of six equations to solve for the following variables:

Φ_1	Solid Phase Potential
Φ_2	Solution Potential
c	Lithium ion concentration in solution
cs	Lithium concentration in the electrode at the electrode/electrolyte interface
i_n	Reaction rate per unit interfacial area
i_2	Solution phase current density

Figure 3 shows a diagram of a porous electrode and where each these variables applies. The separator region contains only electrolyte and a non-active separator material so only solution phase current density and lithium ion concentration in solution are applied there.

The set of equations were originally developed as part of the dualfoil lithium ion battery model developed by Doyle, Fuller, and Newman [23] and take the form outlined in "Mathematical Modeling of Lithium Batteries" by Thomas, Newman, and Darling

[24]. Each of these equations will be briefly discussed with a focus on how they are implemented in the simulation. For more detailed derivations of these equations, see the above sources as well as [26][27].

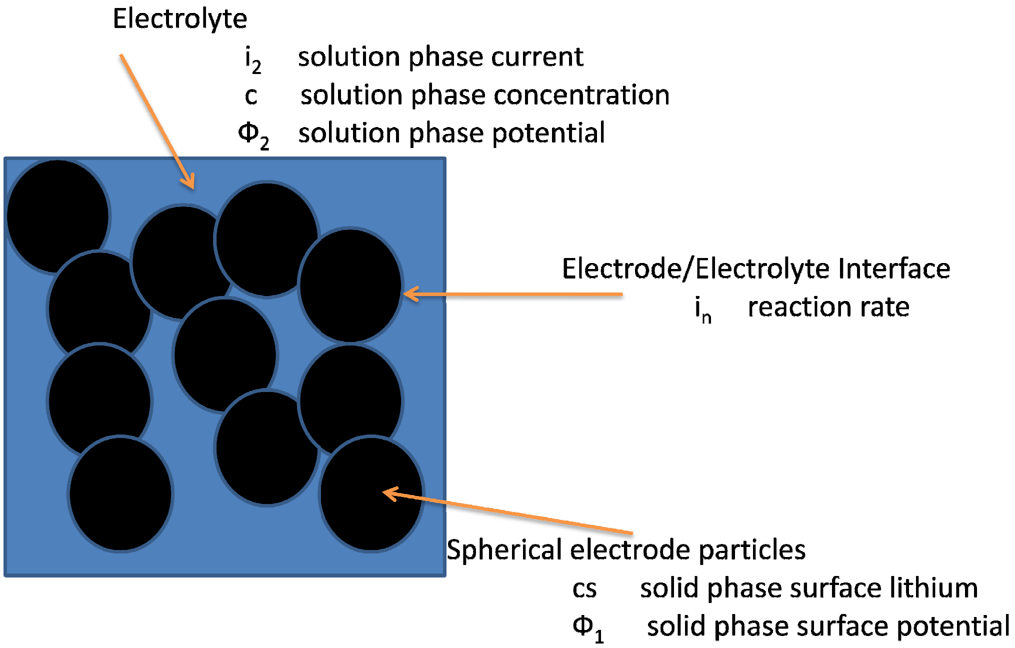

Figure 3: Porous electrode diagram showing where each of the six variables applies.

1.4.2.1 Reaction Rate: Butler-Volmer Equation

The Butler-Volmer equation calculates the rate of reaction per interfacial area (i_n) based on the open circuit potential, solid and solution phase potential, and resistance of the SEI layer (R_{film}), which covers the surface of the graphite anode.

$$i_n = i_o\left[\exp\left(\frac{\alpha_a F\left(\Phi_1 - \Phi_2 - U - i_n R_{film}\right)}{RT}\right) - \exp\left(\frac{-\alpha_c F\left(\Phi_1 - \Phi_2 - U - i_n R_{film}\right)}{RT}\right)\right] \quad [1.5]$$

The overpotential is ($\Phi_1 - \Phi_2 - U$). This is the deviation from the thermodynamic potential between the two electrodes at the given surface concentrations of lithium and drives the rate of reaction of the battery. i_o is the exchange current density, which is the reference current for the system based on the kinetics of the reaction. This varies with both temperature and concentration and the formulation of i_o used in the model for each electrode is described in Appendix A.

1.4.2.2 Li^+ Concentration in Solution: Concentrated Solution Theory

The concentration of Li^+ ions in the electrolyte is calculated from concentrated solution theory. As a result of the electrochemical reactions at the electrode/electrolyte interface of each electrode, Li^+ will enter the electrolyte on one electrode and then diffuse to the other electrode where Li^+ will enter the solid electrode phase. This results in a concentration gradient across the cell. Under very high charge or discharge conditions Li^+ can become depleted at the electrode/electrolyte interface limiting the maximum power of the battery. Because the electrodes are porous, electrolyte exists throughout the entire thickness of both electrodes and the separator region and equation 1.6 applies throughout these three layers of the cell. The concentration of Li^+ in the solution phase is treated as uniform within a control volume.

The full concentrated solution theory diffusion equation from [24] is

$$\varepsilon \frac{\partial c}{\partial t} = \nabla \cdot \varepsilon D \left(1 - \frac{dlnc_o}{dlnc}\right) \nabla c + \frac{t_{-}^{o} \nabla \cdot i_2 + i_2 \cdot \nabla t_{-}^{o}}{z_+ v_+ F} - \nabla \cdot c\mathrm{v}_o + aj_- \qquad [1.6]$$

The first term represents diffusion due to concentration gradients in a concentrated solution, the second term is the reaction rate term, the third term is due to convection in the electrolyte (v_o) and is neglected, and aj_- is the reaction rate for side reactions, which is also neglected.

The boundary conditions are taken to be

$$\frac{\partial c}{\partial x} = 0 \qquad [1.7]$$

at the boundary between each electrode and current collector foil.

1.4.2.3 Li Concentration at the Electrode Surface: Solid Transport in a Sphere/Duhamel's Superposition Integral

The concentration of lithium in the solid phase, the electrode, must also be calculated. The porous electrode is approximated as a collection of evenly sized spheres. The concentration of lithium at the surface of the spheres at the electrode/electrolyte interface needs to be calculated as this will determine the local state of charge and local reaction rates of the battery.

The basic equation for solid transport in a spherical particle is:

$$\frac{\partial c_s}{\partial t} = \frac{1}{r^2}\frac{\partial}{\partial r}\left(D_s r^2 \frac{\partial c_s}{\partial r}\right) \qquad [1.8]$$

with the boundary conditions

$$\left.\frac{\partial c_s}{\partial r}\right|_{r=0} = 0 \qquad [1.9]$$

and

$$-D_s \left.\frac{\partial c_s}{\partial r}\right|_{r=R} = j_{Li^+} \qquad [1.10]$$

where j is the flux of lithium out of the electrode due to the electrochemical reaction and D_s is the diffusion coefficient.

Fully solving the above equation would add another dimension to the model and significantly increase computation time. Instead, a simplification, Duhamel's

Superposition Integral, is applied. This simplification is valid when the solid diffusion coefficient can be approximated as a constant. While not strictly accurate for $LiFePO_4$ electrodes, it is close enough for the purposes of this simulation. The surface concentration is approximated by taking the flux at each time step as a step change in concentration at the surface and damping its effect on concentration at future time steps. In the limit as the time step goes to zero this becomes [24]:

$$\frac{\partial c_s}{\partial r}(R,t) = \int_0^t \frac{\partial c}{\partial t}(R,\delta)\frac{\partial \bar{c_s}}{\partial r}(R,t-\delta)d\delta \qquad [1.11]$$

The discretized version of this equation used in the model is discussed in section 1.6.3.

1.4.2.4 Solid Potential

The solid phase potential (Φ_1) can be determined directly from Ohm's law using the following equation [24] :

$$I - i_2 = -\sigma\nabla\Phi_1 \qquad [1.12]$$

I is the total current entering the 1D electrochemical model and i_2 is the solution phase current. By current conservation, the current in the solid phase plus the current in the solution phase must equal the total current, so that $I-i_2$ is the current in the solid phase. σ is the solid phase conductivity and by Ohm's law $\Delta V = IR$.

The boundary condition for the anode is

$$i_2 = I \qquad [1.13]$$

at the anode-separator interface. In the cathode this is set to

$$i_2 = 0 \qquad [1.14]$$

at the cathode-current collector interface. The solid-phase potential is only defined in the electrodes so is unspecified in the separator region.

1.4.2.5 Solution Potential

The gradient of the potential in solution is calculated from [24] :

$$\nabla\Phi_2 = \frac{i}{\kappa} + \frac{2RT}{F}(1 - t_+^o)\left(1 + \frac{d\ln f_\pm}{d\ln c}\right)\nabla \ln c \qquad [1.15]$$

The potential drop in solution is due both to the current and conductivity in solution (ΔV = IR) as well as the concentration overpotential (the second term on the right hand side of the equation), which arises from having charged ions in solution.

The boundary condition is set to

$$\Phi_2 = 0 \qquad [1.16]$$

at the positive electrode/current collector interface. This boundary condition is defined arbitrarily because potential has no absolute value and is only defined in terms of a potential difference to a reference potential. In the model, this defines both Φ_1 and Φ_2 as the potential difference with respect to the electrolyte at the positive current collector interface.

1.4.2.6 Solution Current

The current in the solution phase (i_2) is calculated from the following equation [24]:

$$\nabla \cdot i_2 = a i_n \qquad [1.17]$$

The divergence of the current is set equal to the reaction rate (i_n), which is defined by the Butler-Volmer equation, shown in section 1.4.2.1, multiplied by the active interfacial area per unit volume.

The boundary condition is

$$i_2 = 0 \qquad [1.18]$$

at the negative electrode/current collector interface.

1.4.2.7 List of Symbols

a	active interfacial area per unit volume
α_a,α_c	anodic and cathodic transfer coefficients (generally taken to be 0.5)
c	salt concentration in electrolyte
c_s	concentration of lithium in the solid phase
D	diffusion coefficient in solution
D_s	solid phase diffusion coefficient
ε	porosity (volume fraction of electrolyte)
F	Faraday's constant (96487 C/equiv)
$f_\pm$	mean molar activity coefficient of the electrolyte
h	mesh space distance
i_2	solution phase current
i_n	transfer current per unit interfacial area
i_o	exchange current density
j	total flux due to electrochemical reaction
κ	solution phase conductivity
N	flux of Li^+

Φ_1	solid phase potential
Φ_2	solution phase potential
R_{film}	SEI layer resistance
R	electrode particle radius
T	temperature
t_+	cation transference number
U	open circuit potential
v_o	electrolyte velocity

1.5 ELECTROCHEMICAL HEAT GENERATION

Electrochemical heat generation can be calculated from the following equation [28]:

$$\dot{Q} = I\left(U - V - T\frac{\partial U}{\partial T}\right) \qquad [1.19]$$

Where Q is the heat generation rate, T is temperature, I is the total current, V is the voltage across the cell, and U is the open circuit potential of the cell, which is determined from the average lithium concentration of each electrode. This equation includes both the irreversible heat generation due to the cell resistance I(U-V) as well as the reversible heat generation -IT(∂U/∂T) due to the entropy of reaction. The first heat generation term is always exothermic and the latter can be exothermic or endothermic depending on the entropy of reaction and whether the battery is being charged or discharged.

The equation neglects the heat of mixing contribution to the overall heat generation. Other equations are available which include heat of mixing across the electrode including [29], but this still neglects the heat of mixing effects within the particles. Calculating the heat of mixing within a particle requires understanding the radial concentration distribution within each particle of the electrode. Because the Duhamel's Superposition Integral approximation is used as a simplification for the solid phase lithium concentration, as discussed in section 1.4.2.3, only the surface concentration of lithium is known for each control volume. This prevents full calculation of heat of mixing effects in the battery. Rather than inconsistently treating heat of mixing by including it across the electrode, but not within the particles, heat of mixing is neglected entirely in the simulation. For a discussion of the error this may cause based on electrode parameters and discharge rates see Thomas and Newman "Thermal Modeling of Porous Insertion Electrodes" [30]

1.6 NUMERICAL METHOD

The previously described six electrochemical equations (1.5, 1.6, 1.11, 1.12, 1.15, 1.17), some of which are non-linear partial differential equations, are converted to finite-difference approximations and then solved using the Newton-Raphson method as described in *Electrochemical Systems* [26]. Both the solid and solution phase concentration equations (1.6, 1.11) are solved using slightly different methodologies as discussed in sections 1.6.2 and 1.6.3. The differential equations are discretized in one dimension for a slab configuration with the exception of solid diffusion, which takes place in the spherical electrode particles.

1.6.1 Finite Difference Method

With the finite difference method, differentials are converted as follows:

$$\left.\frac{dc}{dx}\right|_{j-1/2} = \frac{c(j)- c(j-1)}{2h} + O(h^2) \qquad [1.20]$$

$$\left.\frac{d^2c}{dx^2}\right|_{j} = \frac{c(j+1)+ c(j-1)-2c(j)}{h^2} + O(h^2) \qquad [1.21]$$

For differential equations with respect to time, the Crank-Nicolson method, which is implicit and unconditionally stable with respect to time, is applied. As an example, for a simplified version of the diffusion equation used in the model, this would take the form:

$$\frac{\partial c}{\partial t} = D\frac{\partial^2 c}{\partial x^2} \qquad [1.22]$$

$$\frac{c_j^{n+1}-c_j^n}{\Delta t} = \frac{1}{2}\left(D_j^{n+1}\frac{c_{j+1}^{n+1}+c_{j-1}^{n+1}-2c_j^{n+1}}{h^2} + D_j^n\frac{c_{j+1}^n+c_{j-1}^n-2c_j^n}{h^2}\right) \qquad [1.23]$$

Where n is the time step, j is the mesh point, h is the mesh spacing, Δt is the time step size, c is the variable being solved, and D is a coefficient that can vary in time and space.

1.6.2 Solution Phase Concentration Control Volume Method

The solution phase concentration equation is solved using the control volume method where

$$\frac{\Delta c}{\Delta t} = flux\ in - flux\ out + reaction\ rate \qquad [1.24]$$

As an example, for the case of mesh point j at the separator/cathode interface this is constructed as follows based on the derivation from [27]

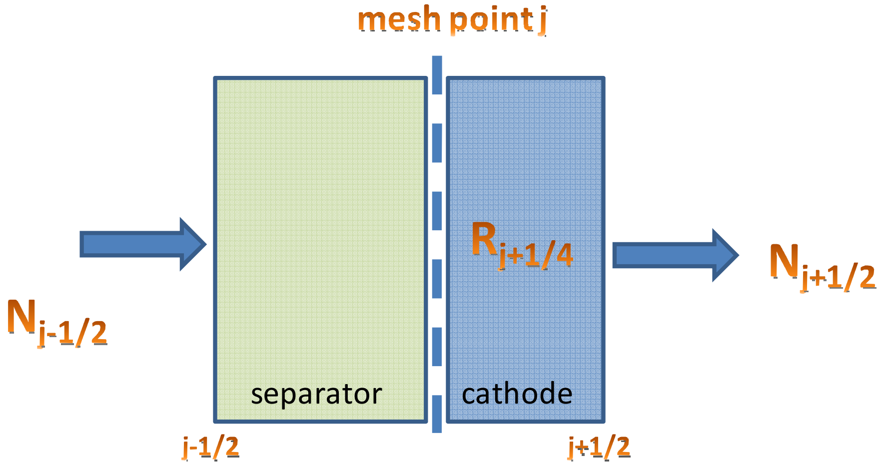

Figure 4: Control volume formulation

Overall control volume expression:

$$\varepsilon_{sep} h_{sep}\left(\frac{3c_j^{t+1} + c_{j-1}^{t+1} - 3c_j^t + c_{j-1}^t}{4\Delta t}\right) + \varepsilon_{cat} h_{cat}\left(\frac{3c_j^{t+1} + c_{j+1}^{t+1} - 3c_j^t + c_{j+1}^t}{4\Delta t}\right) =$$

$$\left(N_{j-1/2}^{t+1} - N_{j+1/2}^{t+1}\right) + \left(N_{j-1/2}^{t} - N_{j+1/2}^{t}\right) + R_{j+1/4}^{t+1} + R_{j+1/4}^{t} \qquad [1.25]$$

Reaction rate in the right control volume:

$$R_{j+1/4} = \frac{a}{8}\left(3i_{n,j} + i_{n,j+1}\right) h_{cat} \qquad [1.26]$$

Flux out on the right side:

$$N_{j+\frac{1}{2}} = \varepsilon_{cat} D_{j+1/2}\left(1 - \frac{dlnc_o}{dlnc}\right)\left(\frac{c_{j+1} - c_j}{h_{cat}}\right) + \frac{t_{+,j+1/2}^{o}}{F}\left(\frac{i_{2,j+1} + i_{2,j}}{2}\right) \qquad [1.27]$$

1.6.3 Discretization of Duhamel's Superposition Integral

The continuous version of Duhamel's superposition integral (Equation 1.11) is discretized as follows for usage in the model:

$$\left.\frac{\partial c_s}{\partial r}\right|_{R,t_n} = \frac{(c_{s,n} - c_{s,n-1})}{\Delta t} A_1 + \sum_{j=0}^{n-2} \frac{(c_{s,j+1} - c_{s,j})}{\Delta t} A_{n-j} \qquad [1.28]$$

$$A_n = \frac{a(t_n) - a(t_{n-1})}{D_s} R$$

$$a(\tau) = \frac{2}{\pi^2} \sum_{n=1}^{\infty} \frac{1}{n^2} [1 - \exp{(-n^2 \pi^2 \tau)}]$$

$$\tau = \frac{t D_s}{R}$$

Where c_s is lithium concentration in the solid phase, R is the electrode particle radius, D_s is the diffusion coefficient of lithium in the electrode, and t is time. The above series is expanded until within a specified user-defined error, which is generally taken to be < 0.01% change in going to the next step in the series. The full derivation is provided in [24] and is based on a Laplace transform of Equation 1.11.

1.6.4 Newton-Raphson Numerical Method

The iterative Newton-Raphson method is then used to solve a discretized version of the original set of non-linear electrochemical equations (1.5, 1.6, 1.11, 1.12, 1.15, 1.17). The Newton-Raphson method is also used for solving the set of non-linear equations for the thermal model and the 3D current distributions, as will be discussed in Chapter 2. With the Newton-Raphson method an initial guess is applied and successive approximation leads to quadratic convergence onto the solution based on the slope of the curve at the current guess. Given the highly non-linear nature of the equations in the model, a good initial guess is essential to get convergence. The specific methodology applied to this model to achieve good initial guesses will be discussed in more detail in Chapter 2.

For the Newton-Raphson, method a Taylor series expansion is taken around an initial guess c^o

$$g(c) = g(c^o) + \left.\frac{dg}{dc}\right|_o (c - c^o) + \cdots \qquad [1.29]$$

It then follows that

$$c - c^o = \Delta c = -\frac{g(c^o)}{dg/dc|_o} \qquad [1.30]$$

Where c is now a closer approximation to the solution from the prior guess of c^o. This is expanded to a multidimensional Taylor series in matrix form that is comprised of discretized versions of the set of six electrochemical equations (1.5, 1.6, 1.11, 1.12, 1.15, 1.17) applied to all of the mesh spaces in the electrochemical battery model. As described in *Electrochemical Systems* [26]:

$$\sum_k A^o_{i,k}\Delta C_{k,j-1} + B^o_{i,k}\Delta C_{k,j} + D^o_{i,k}\Delta C_{k,j+1} = g^o_{i,j} \qquad [1.31]$$

$$A^o_{i,k} = -\frac{\partial g^o_{i,j}}{\partial C_{k,j-1}}, \quad B^o_{i,k} = -\frac{\partial g^o_{i,j}}{\partial C_{k,j}}, \quad D^o_{i,k} = -\frac{\partial g^o_{i,j}}{\partial C_{k,j+1}} \qquad [1.32]$$

Where k is each of the six unknown variables to be solved for and j is a mesh point in the model.

In matrix form [26] this becomes:

$$\begin{bmatrix} B(1) & D(1) & & & & \\ A(2) & B(2) & D(2) & & 0 & \\ & A(3) & B(3) & & & \\ & & & \ddots & & \\ & 0 & & A(nj-1) & B(nj-1) & D(nj-1) \\ & & & & A(nj) & B(nj) \end{bmatrix} \Delta C = \mathrm{G} \qquad [1.33]$$

Where A, B, and D are 6x6 submatrices for the six electrochemical equations applied. The overall matrix is square with the size determined by the number of electrochemical equations, six, multiplied by the total number of mesh spaces in the 1D model. The system is solved for ΔC, which is added to the prior guess for each of the unknown variables to gain a closer approximation to the solution. G is the value of each of the equations at the current approximation for each variable, and the system is converged as G approaches zero.

The matrices generated from this method are solved using matrix division in MATLAB where

$$\Delta C = \frac{M}{G} \qquad [1.34]$$

and MATLAB determines the most efficient way to solve the equation based on the matrix structure.

Chapter 2: Model Structure

2.1 DETERMINING CURRENT DISTRIBUTIONS

One of the challenges in developing a 3D thermal-electrochemical battery model is determining the current distributions in three dimensions throughout the system. The 1-dimensional electrochemical model requires the specification of either a total current into the system or a total potential difference between the current collector foils on the positive and negative electrodes. In the case of a full 3D battery cell, only the total voltage, total current or total power at the current collector tabs is specified; the local current and potential difference between adjacent negative and positive current collectors is unknown. These values can vary quite substantially throughout the system.

Converting the set of electrochemical equations into three dimensions and fully solving for the system would be computationally intensive. It would also be difficult to reliably get convergence given the highly non-linear nature of some of the equations. Instead the problem is handled by converting the current collector foils into a network of resistors and utilizing the 1D electrochemical model to develop an equation for how current varies with voltage across the electrochemical cell.

The concept of converting the battery into a network of resistors has been previously proposed by Tiedemann and Newman for lead acid battery grids [31]. They discussed using a constant transfer resistance across the cell as well as fitting an equation to experimental or model output data.

In order to determine the 3D current distribution in our model, the overall battery cell is converted into a grid of 1D electrochemical models as shown in Figure 5. The electrochemical models use porous-electrode theory developed for lithium ion batteries by Doyle, Fuller and Newman [23] as discussed in Chapter 1. These models solve the battery cell for the following six parameters: solution phase lithium ion concentration, solid phase lithium concentration, solution current, reaction rate, solid potential, and solution potential. The current collector plates are treated as 2D networks of standard resistors that vary with temperature. All of the current is assumed to be redistributed in the current collector foils and then to travel perpendicular to the cell through the other battery layers. This should be a reasonable assumption given that the current collector foils are orders of magnitude more conductive than the other layers of the cell (see Appendix A for material property data).

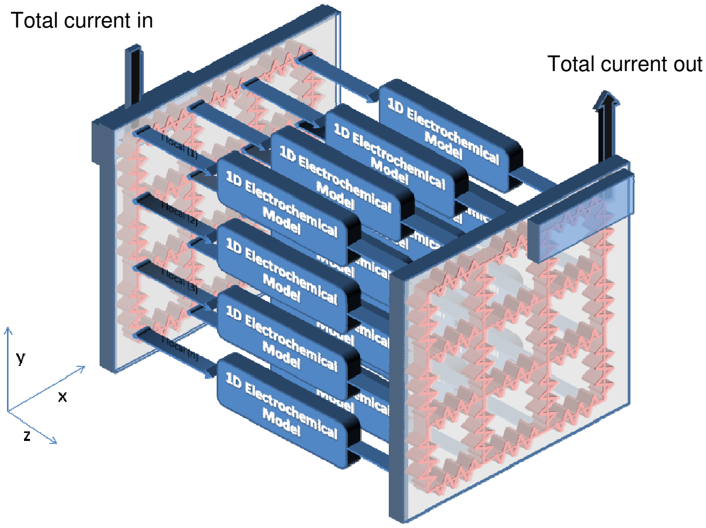

Figure 5: Schematic of overall model structure. Current collector foils are treated as a 2D network of resistors and the electrochemical cell is made up of a grid of 1D electrochemical models. The current enters and leaves the battery through the current collector tabs specified at specific nodes on the battery.

To determine the current distribution between the electrochemical nodes, each 1D electrochemical model is replaced by a variable non-linear resistor, as shown in Figure 6, representing the local I-V curve of the electrochemical cell. This I-V curve varies in both time and space in the model and is calculated directly from the electrochemical simulations, as will be discussed in section 2.2.

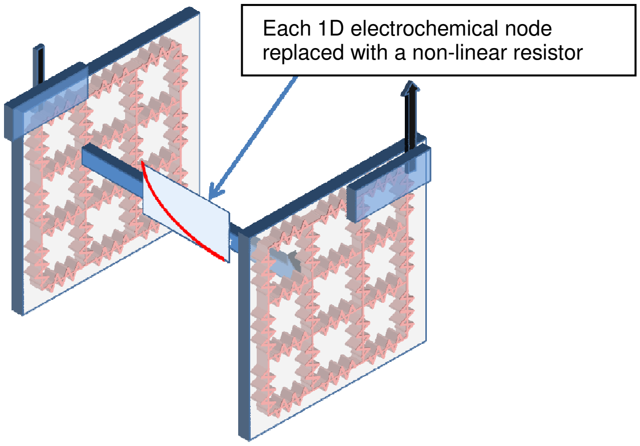

Figure 6: Schematic of model structure showing a 1D electrochemical model replaced with an I-V curve. Each 1D electrochemical model is replaced, which would result in 16 different curves in this example.

Using this framework and applying current conservation, which states that the current entering each node on the current collector plate must equal the current exiting each node (as shown in Figure 7 and Equation 2.1) the current into each of the 1D electrochemical models can be calculated.

$$I_{x-1} + I_{y-1} = I_{x+1} + I_{y+1} + I_{Electrochem,x,y} \qquad [2.1]$$

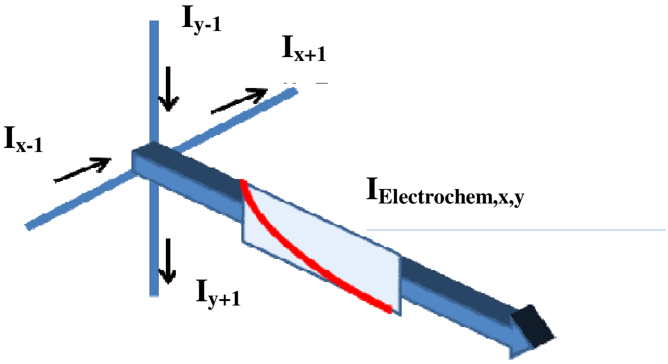

Figure 7: Schematic of current flow at each current collector node.

From Equation 2.1, a system of non-linear equations is generated to determine the overall current distribution within a battery cell. This set of equations is applied to each node on each current collector plate. For a battery with 4x4 electrochemical nodes as shown in Figure 5, this would result in a system of 32 equations with 16 on each current collector plate.

From Ohm's law, for current in the plane of the current collector plate:

$$I_{x-1,y} = \frac{(V_{x-1,y} - V_{x,y})}{R} \qquad [2.2]$$

Where $V_{x,y}$ is the voltage of the node on the current collector at position (x,y), R is the temperature dependent resistance of the current collector foil between the two nodes, and I is the current between the two nodes.

$I_{Electrochem,x,y}$ is the electrochemical current through the battery cell at node (x,y). This is defined as a cubic fit to the I-V relationship of the electrochemical model for that node.

$$I_{Electrochem,x,y} = A(\Delta V_{x,y})^3 + B(\Delta V_{x,y})^2 + C(\Delta V_{x,y}) + \mathrm{D} \qquad [2.3]$$

Where $\Delta V_{x,y}$ is the potential difference between the anode and cathode current collector foils at (x,y), located directly opposite each other, and A,B,C,D are coefficients determined by curve fitting to the I-V profile of that node, as will be explained in section 2.2. Any number of curve fits could be used, but a cubic fit is chosen as it produces a low R^2 value over a range of conditions and is computationally efficient.

This results in a series of non-linear equations that are solved using the Newton-Raphson method to obtain the voltage at each current collector node in the battery. The anode and current collector tabs provide the boundary conditions. The anode tab is taken to be the reference voltage of $V = 0$ and the cathode tab specified as the overall voltage of the battery. Once the voltages are determined at all points on the current collector plates, the current into each electrochemical node is determined from Equation 2.3. Each 1D electrochemical model node is then fully solved at the current time step with the local current as the input. Variations for power and current control are discussed in section 2.3.

In the case of a prismatic cell stack, this methodology can be expanded, linking all of the cells together and applying nodal analysis to the entire system. In this case, current from the current collector plates can go into either the cell on the left or the right, as shown in Figure 8, because the cells are electrically in parallel.

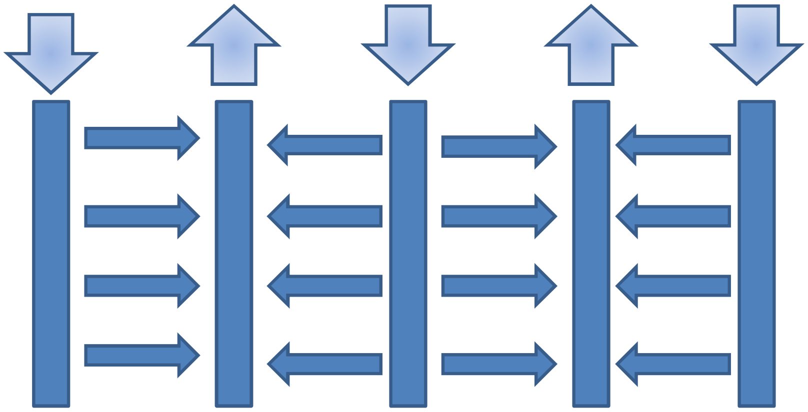

Figure 8: Diagram of current pathways in a cell stack

All of the anode current collector tabs are again specified to be at the same reference voltage of zero and the cathode current collector tabs are all at the same specified overall voltage of the battery. This allows for further determination of current distributions between cells in a stack and the corresponding coupled temperature effects.

2.2 ELECTROCHEMICAL CURRENT-VOLTAGE RELATIONSHIP

The electrochemical current as a function of voltage is determined by running each electrochemical node at several current densities over the same time step to determine the voltage drop for each current, as shown in Figure 9. A cubic curve fit is applied to the results to obtain Equation 2.3, which is used to solve for the current distribution in the battery as previously discussed.

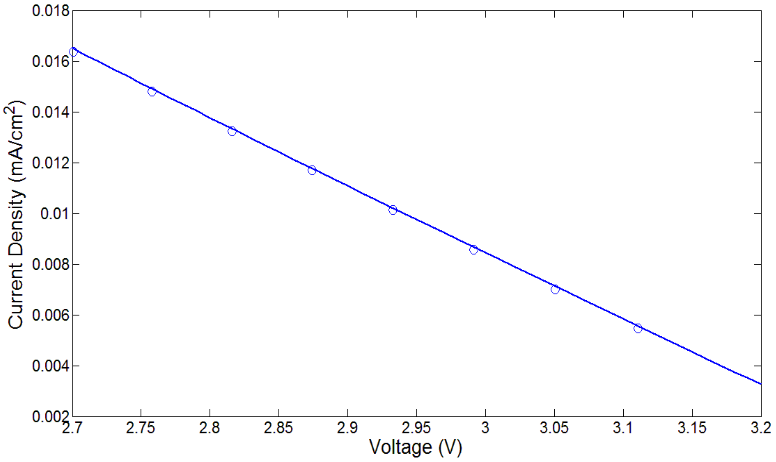

Figure 9: Curve fit to obtain equation for how current varies as a function of voltage across the 1D electrochemical cell. This curve fit is for a particular state of charge, temperature, and concentration profile and will change over both time and space in the battery.

During discharge, as lithium is transported from anode to cathode, the current will drop for a given voltage level resulting in a shifting downward of the current-voltage curves as seen in Figure 10.

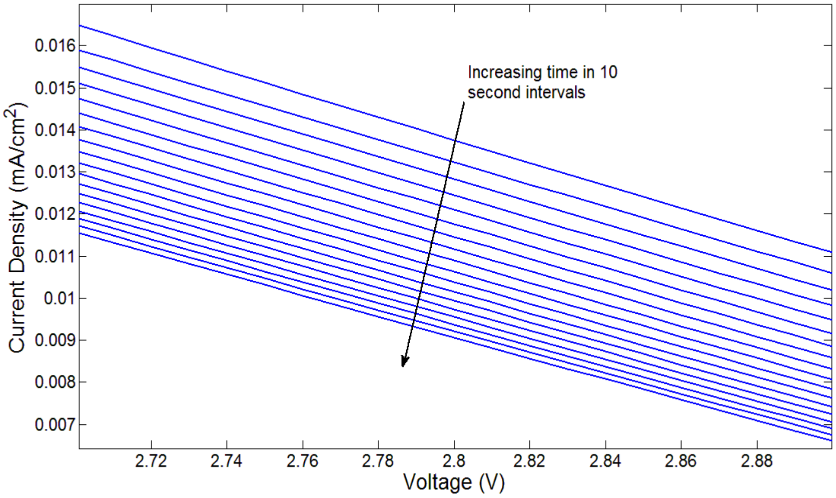

Figure 10: Changing I-V profile over time during a 5C discharge

To save on the computational time that would be involved in running all of the electrochemical nodes multiple times at each time step, this shift downward can be approximated from the drop in current for a given voltage over the prior time step. This ΔI is applied to shift the entire curve downward while the shape of the curve is kept constant. Each 1D electrochemical model then needs to be run only once at each time step to solve for the six variables (solid and solution concentration, solid and solution potential, reaction rate, and solution phase current) rather than multiple times at different currents to also generate a new I-V curve.

The model checks for the accuracy of the predicted curve fit by comparing the voltage drop between the anode and cathode current collectors for a given current density, as calculated from the electrochemical model, with the current predicted by the cubic fit at the same ΔV. If this error is outside of a specified threshold, then the cubic fits are recalculated for all of the nodes in the battery by running each 1D electrochemical node at multiple currents. This approximation compares favorably with the condition of running the current sweep at every time step, while significantly reducing computational time.

2.3 POWER AND CURRENT CONTROL

Using the previously described nodal analysis framework, it is straightforward to implement power and current control in the model. In the case of current or power control, the cathode current collector tab voltage becomes an unknown. An additional equation is added to the system of equations which specifies that the sum of the currents leaving all tabs on the cathode must equal the total current specified for the battery:

$$I_{batt} = \sum_{n=1}^{\#electrode\ tabs} I_{tab,n} \qquad [2.4]$$

For power control, a second additional equation is required:

$$P_{batt} = I_{batt} * V_{batt} \qquad [2.5]$$

and the full system of equations is solved as before using the Newton-Raphson numerical method.

2.4 THERMAL-ELECTROCHEMICAL MODEL COUPLING

Coupling is required between a thermal model and an electrochemical model to determine temperatures throughout the battery and the impact of temperature changes on electrochemical performance. The electrochemical-thermal model is coupled in a similar way to the methodology described by Song and Evans [6], which assumes quasi steady-state temperature over a given time step. At the end of each time step, the heat generation rate is calculated for each node from both the electrochemical results (Equation 1.19) and from resistive heating in the current collector foils (Equation 2.6). The thermal model uses the heat generation data to determine temperature distributions throughout the battery for the next time step taking into account heat capacity and heat transfer within the battery and between the battery and the surroundings.

Resistive heating in the current collector foils is treated as follows:

$$\dot{Q} = 0.5\left[\frac{\left(V_{x,y} - V_{x-1,y}\right)^2}{R_{x-\frac{1}{2},y}} + \frac{\left(V_{x,y} - V_{x+1,y}\right)^2}{R_{x+\frac{1}{2},y}} + \frac{\left(V_{x,y} - V_{x,y-1}\right)^2}{R_{x,y-\frac{1}{2}}} + \frac{\left(V_{x,y} - V_{x,y+1}\right)^2}{R_{x,y+\frac{1}{2}}}\right]$$

[2.6]

Where $V_{x,y}$ is the voltage on the current collector in the center of node (x,y) and R is the local current collector resistance, which varies based on local temperature. The new local temperature at each node is then calculated based on the local heat generation rate and heat transfer between nodes and to the surroundings.

Heat transfer between nodes is based on a standard heat conduction equation:

$$\rho C_p \frac{\partial T}{\partial t} = k_x \frac{\partial^2 T}{\partial x^2} + k_y \frac{\partial^2 T}{\partial y^2} + k_z \frac{\partial^2 T}{\partial y^2} \quad [2.7]$$

Where k is the thermal conductivity, T is temperature, t is time, ρ is density and C_p is heat capacity. The x and y direction are in the plane of the current collector and the z direction is between cells in a stack. As a result, k_x and k_y are calculated for the battery layers (current collector foils, electrodes, and separator) being in parallel and k_z for the layers being in series.

For k_x and k_y the effective thermal conductivity is the sum of the conductivity of each layer times its volume fraction.

$$k_x = k_y = \sum_{i=1}^{5} k_i f_i$$

[2.8]

For k_z the effective thermal conductivity is the inverse sum of the conductivities of each layer times the volume fraction.

$$\frac{1}{k_z} = \sum_{i=1}^{5} \frac{f_i}{k_i}$$

[2.9]

The model allows for both convective and radiative heat transfer to the surroundings:

$$\dot{q}_{conv} = h(T_{node} - T_{amb}) \qquad [2.10]$$

$$\dot{q}_{rad} = \sigma E(T_{node}^4 - T_{amb}^4) \qquad [2.11]$$

Where q is the heat transfer rate from the battery node to the surroundings per unit area, T_{node} is the temperature of that node in the battery, T_{amb} is the ambient temperature, h is the convective heat transfer coefficient in (W/cm^2 K), E is the emissivity, and σ is the Stefan-Boltzmann constant. The heat transfer coefficient (h) and the emissivity (E) are user defined constants that are specified for each of the six faces of the battery. Conductive heat transfer to the surroundings, which primarily takes place through the current collector tabs, may be added in a future update to the model. Conductive heat transfer can be approximated by adjusting h for some faces of the battery.

The temperature is considered constant across the five battery layers, but will vary in the plane of the current collector and between cells in a cell stack. This approximation is considered reasonable as a single cell, which has a thickness of around 0.03 centimeters, is thermally thin [30].

Similar to the solution of the electrochemical equations, the above equation is converted to a finite difference approximation and solved in matrix form using the Newton-Raphson numerical method as discussed in section 1.6.4. From this solution, the temperature at each node in the battery is calculated. The temperature then influences the electrochemical performance at the next time step.

In addition, the model checks that the change in temperature over a given time step is within a user-defined threshold (generally ~2-3K). If the temperature change is outside of this threshold, the model is rerun over the given time step with the temperature taken as the average of the temperature at the start of the time step and the temperature that was calculated for the end of the time step.

2.5 Improving Convergence Stability

Convergence can be difficult due to the highly non-linear nature of some of the equations, particularly if material properties, such as diffusivity or conductivity, vary strongly with temperature or concentration. Convergence is particularly challenging on the first time step as a good initial guess is required to enable the model to reach a converged solution. To handle these difficulties, the model starts at an initially low current value, which is in the linear range of Butler-Volmer electrode kinetics, and then geometrically increases the current, using the prior current as an initial guess, until the desired current level is reached as seen in Figure 11. A set of linear equations are solved at the initially low current value (with a starting current generally set to ~0.001% of the final target current level) to generate initial guesses for a full solution using the Newton-Raphson method.

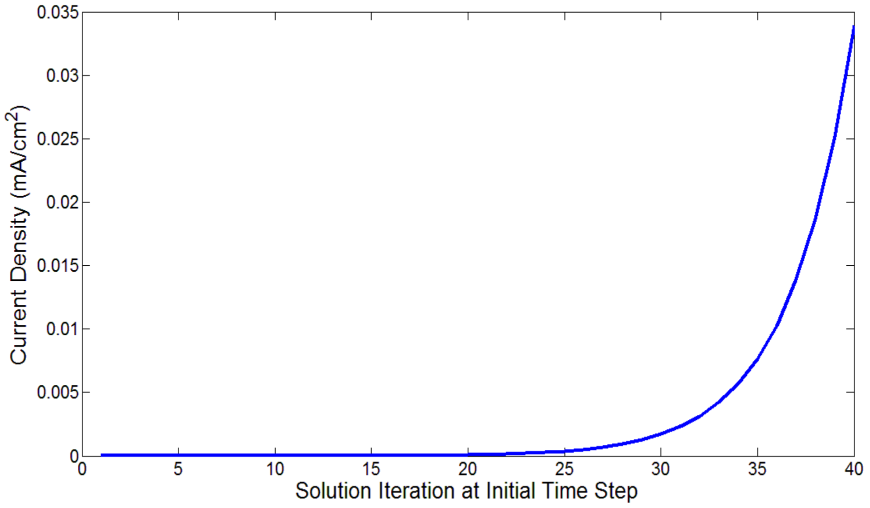

Figure 11: Current sweep at the start of simulation to aid in convergence

On subsequent time steps, the values from the prior steps are used as an initial guess. Applying a variable time step would aid in convergence stability in this case, but has not yet been implemented in the model.

2.6 MATERIAL PROPERTY DATA

The model requires a large set of physical property data for each of the five battery cell layers. Many of these parameters vary with temperature and/or concentration. All of the data used in the simulation were gathered from various sources in the literature. As such, the simulation results are indicative of a representative lithium ion battery cell with lithium graphite and lithium iron phosphate electrodes as opposed to a specific experimental cell to which these results were matched.

The full set of material property data used in the simulation results are shown in Appendix A. By varying this set of data the model can be used to simulate various lithium ion battery chemistries and configurations.

Chapter 3: Model Results

The 3D thermal-electrochemical battery model has been used to investigate several areas important to battery development including:

- transient 3D current density distribution coupled with thermal effects
- design optimization of current collector thickness and tab placement
- lithium plating on the anode in three dimensions

The following simulations are modeled with a 20x30cm size single cell battery with a 4cm wide tab on each positive and negative current collector foil. The simulations are run with (20x30) nodes in the plane of the current collector foils and 25 mesh points across the thickness of the electrochemical cell. Increasing the number of nodes, mesh spaces, and time steps further is found to have minimal impact on the results as shown in Appendix B. The full set of material property data and design parameters used for the battery simulations can be found in Appendix A. Most of the simulation results are run at high discharge rates to simulate the types of power levels seen in hybrid electric vehicle operation.

3.1 COMPARISON TO EXPERIMENTAL RESULTS FROM THE LITERATURE

To verify that the model is generating results representative of a lithium graphite/lithium iron phosphate cell, a cell discharge cycle was compared to some experimental results in the literature. The material property data (Appendix A) used to simulate the cell was compiled from a variety of sources in the literature, so can be considered representative of a typical $LiC_6/LiFePO_4$ cell as opposed to being fit to a specific cell configuration. Figure 12 compares simulated discharge curves from the model for an isothermal discharge at various C-rates with experimental data from Shim and Striebel [32]. The exact design parameters of the experimental cell are unknown, but the values chosen for the model are likely to be representative. The simulation results match the overall voltage trends from the experimental data for discharge rate and capacity. The overall voltages are slightly higher than the experimental data, but well within the voltage range of other experimental data from the literature, which can be up to 0.3V higher [33][34] than the experimental data shown below.

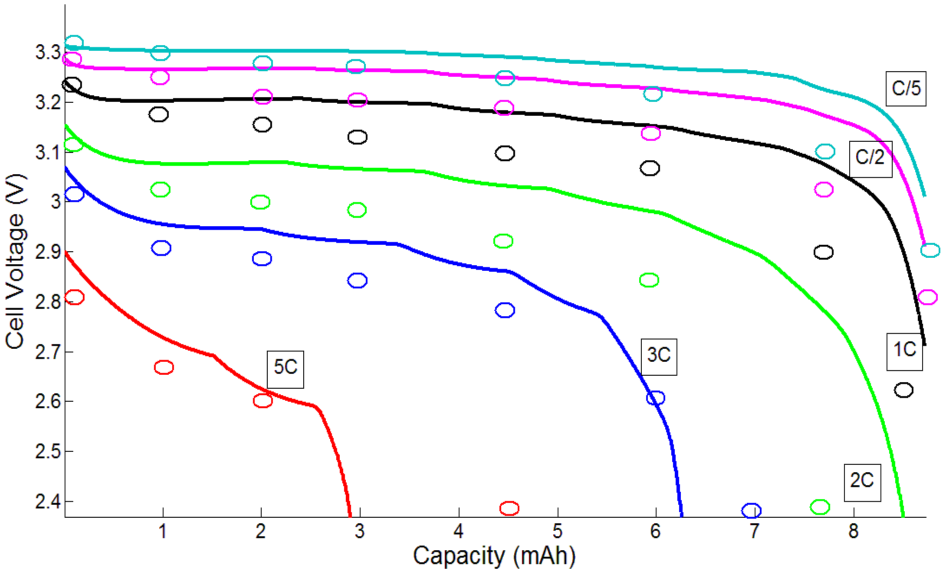

Figure 12: Comparison of model discharge results (solid lines) with experimental discharge data (ovals) from Shim and Striebel [32]

3.2 CURRENT DISTRIBUTION

The 3D thermal-electrochemical model is used to investigate current distributions throughout a battery cell and how these change over time. Understanding the current distribution is important for safety and long term durability. Highly non-uniform current distributions can lead to excessive localized heating, non-uniformities in state of charge, or increased risk of lithium plating.

The following set of simulations are run with a cell discharged at a 5C rate (1C is a full discharge in 1 hour, based upon theoretical capacity, so 5C is a full discharge in 12 minutes). The aluminum current collector foil is set to 10μm thick (shared by two cells in a stack) and the copper current collector is set to a thickness that gives equal conductivity to the aluminum current collector foil at 298K.

Figure 13 shows the local current density distribution in mA/cm^2 as measured by the current distribution between the 1D electrochemical numerical nodes in the battery (see section 2.1 for a full discussion on how current distribution is calculated). This represents the current distribution in the plane of the separator of the battery cell. The arrows represent the anode and cathode current collector tabs. Each foil has one 4cm wide current collector tab located on the bottom edge one quarter from the side as shown in Figure 13.

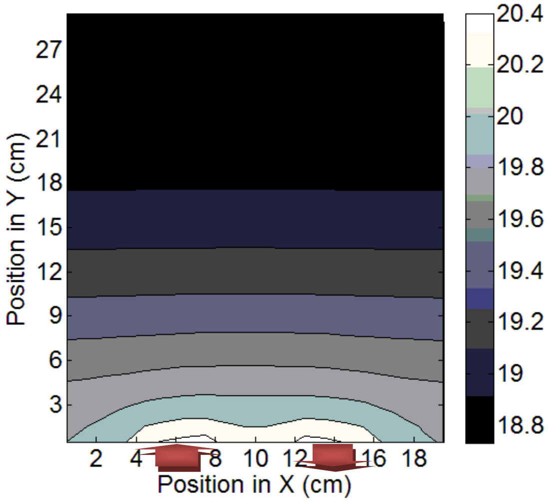

Figure 13: Local current density distribution in mA/cm^2. At the start of a 5C discharge. Red arrows indicate current collector tab position, one 4cm wide tab on each current collector. Max current is 9.4% above minimum current.

At the start of discharge, the maximum current density, which is located at the tabs, is 20.4 mA/cm^2, which is 9.4% higher than the minimum current density located on the opposite edge of the battery.

3.2.1 Transient Current Distribution in Isothermal Versus Adiabatic Conditions

The transient response can also be simulated to see how the current distribution evolves over time. Figure 14 shows the current distribution in the same battery after 30 seconds of discharge under isothermal conditions (so all temperature effects are neglected). The maximum current is now only 7.1% above the minimum as the changes in local concentration in the solid and solution phase over time have led to greater current uniformity.

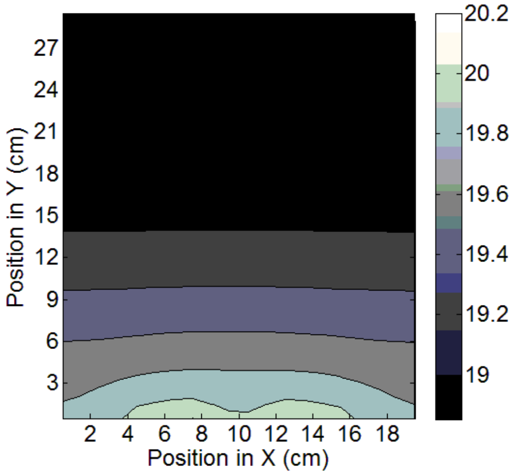

Figure 14: Local current density distribution in mA/cm^2 after 30 seconds of isothermal discharge at a 5C rate. Maximum current is 7.1% above the minimum current.

Simulating the battery under adiabatic conditions results in the current distribution shown below in Figure 15. In this case the maximum current is 21 mA/cm^2, 12.4% above the minimum current, which is more non-uniform than at the start of discharge. The higher heat generation rates near the current collector tabs, due to both ohmic heating in the foil and higher electrochemical rates of reaction, drive higher temperatures at the tabs (as seen in Figure 16). Higher temperatures lower the effective resistance of the electrochemical cell and lead to higher current flow to those parts of the battery. A number of the material properties including diffusivity and conductivity increase with temperature as does the exchange current density, all of which lead to greater current flow to the parts of the battery at higher temperatures. These results show the importance of incorporating the thermal effects in determining current distribution in the battery.

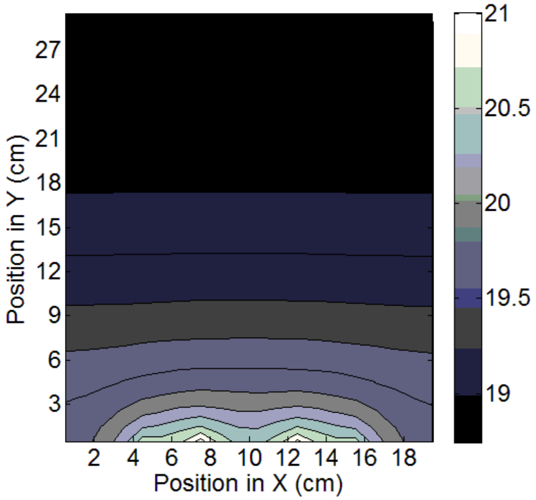

Figure 15: Local current density distribution in mA/cm^2 after 30 seconds of 5C discharge under adiabatic conditions. The maximum current is 12.4% above the minimum current.

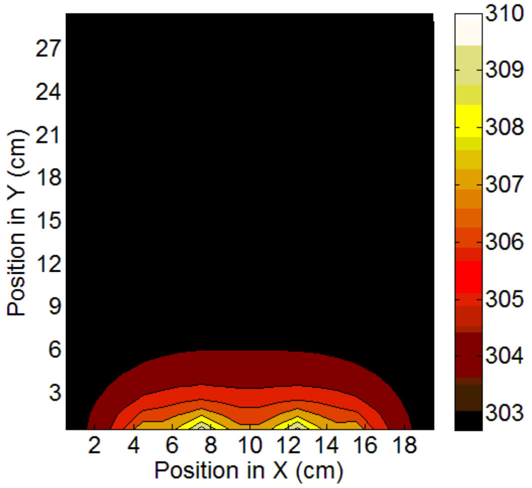

Figure 16: Temperature in Kelvin after 30 seconds of adiabatic discharge at 5C.

3.2.2 Current Distributions and Cooling System Design

These thermal effects lead to the question of how cooling system design can influence current distribution in a battery. Two simple cases are compared: liquid cooling on the same side as the current collector tabs and liquid cooling on the opposite side of the battery of the current collector tabs. Figure 17 shows the temperature distribution after 30 seconds of discharge with liquid cooling on the same side as the current collector tabs and Figure 18 shows the temperature distribution with liquid cooling on the opposite side as the current collector tabs. For both cases the heat transfer coefficient (h) is set to 0.1 W/cm^2 K and occurs just along the top or bottom edge of the cell, which is 20cm by .03 cm in area.

Cooling on the same side as the tabs reduces the temperature non-uniformity in the cell as seen in Figure 17, and thereby results in a more uniform current distribution than in the adiabatic case. In this case, the maximum current is 10.2% above the minimum current after 30 seconds of discharge as seen in Figure 19. Cooling on the opposite side of the tabs leads to an even more non-uniform temperature (Figure 18) and current distribution. In this case, the maximum current is 13.4% above the minimum current after 30 seconds of discharge as seen in Figure 20.

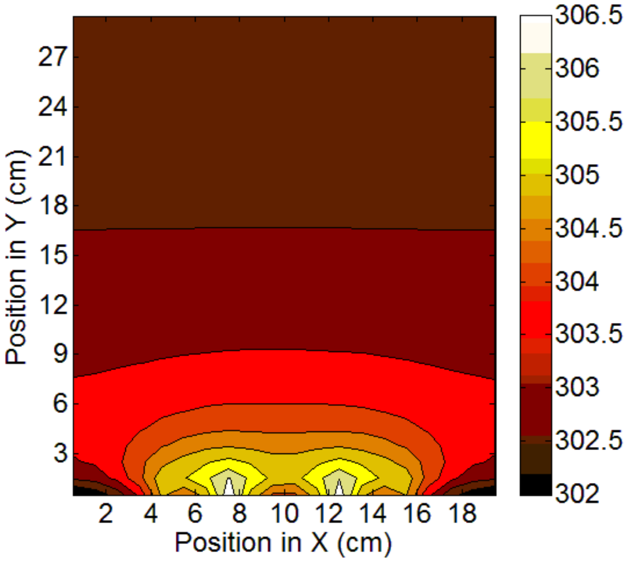

Figure 17: Temperature profile after 30 seconds of discharge at a 5C rate with liquid cooling on the same side as the current collector tabs

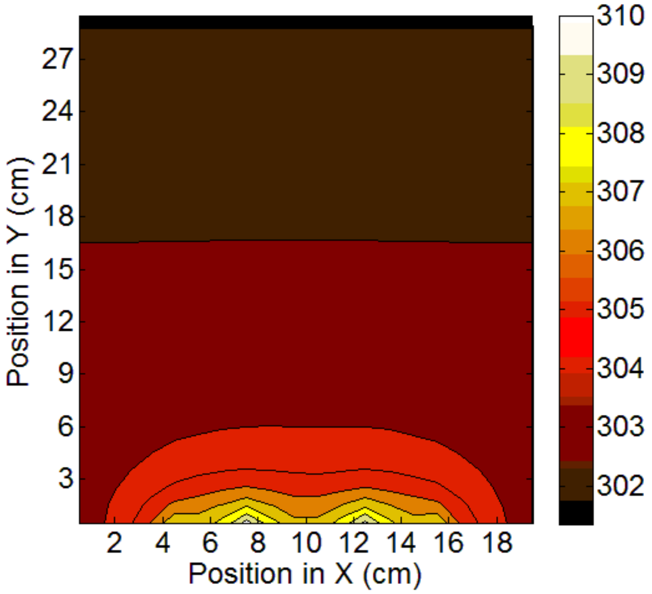

Figure 18: Temperature profile in Kelvin after 30 seconds of adiabatic discharge at 5C rate with liquid cooling on the opposite side of the current collector tabs.

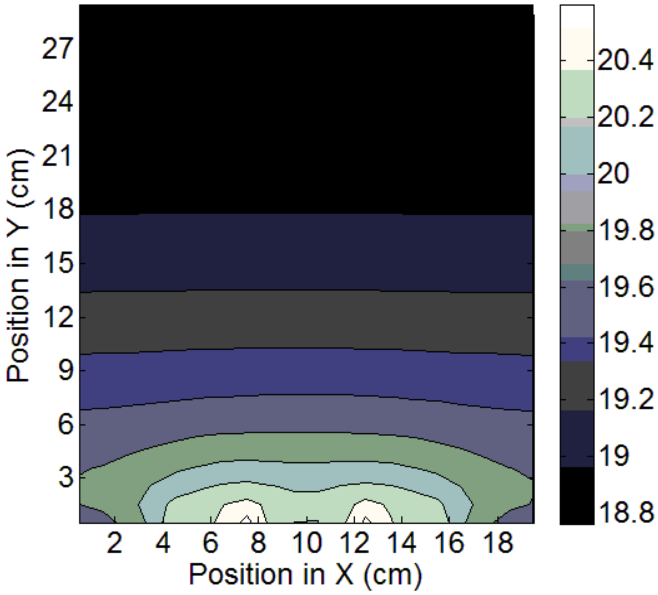

Figure 19: Local current density in mA/cm^2 after 30 seconds of discharge at a 5C rate with liquid cooling on the same side as the current collector tabs. Max current is 10.2% above minimum.

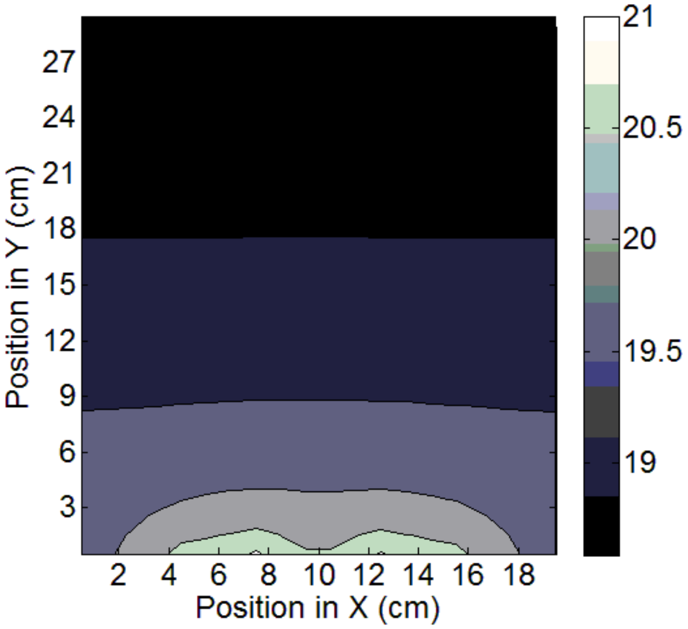

Figure 20: Local current density in mA/cm^2 after 30 seconds of discharge at a 5C rate with liquid cooling on the opposite side of the current collector tabs. Max current is 13.4% above minimum.

These four cases: isothermal, adiabatic, cooling same side as tabs, and cooling opposite side from tabs are compared over a 60 second 5C discharge. The maximum current density divided by the minimum current density in the battery are plotted for these four cases in Figure 21.

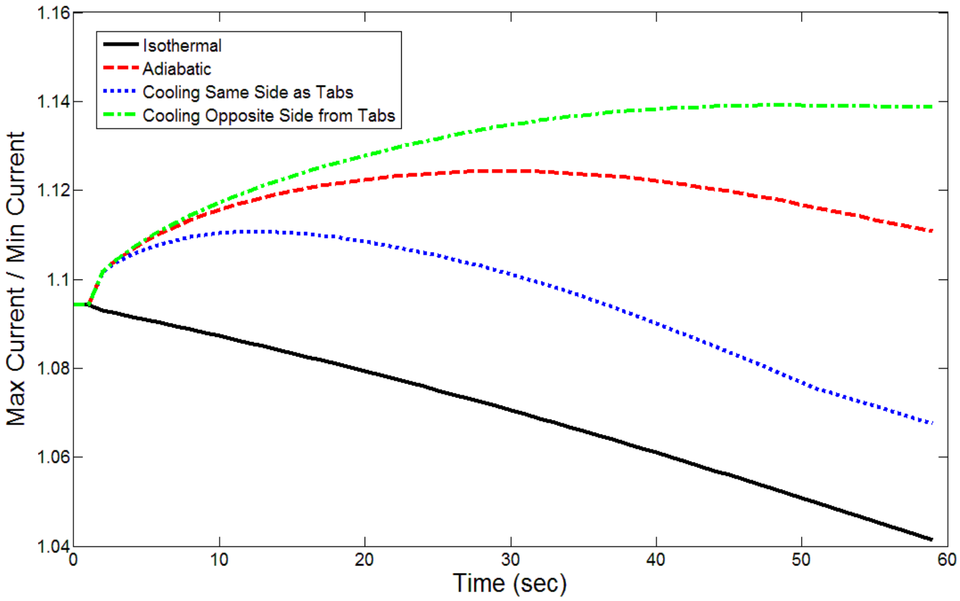

Figure 21: Maximum local current density divided by minimum local current density over a 60 second discharge at a 5C rate.

For the isothermal case, the maximum current density divided by the minimum current density decreases at a fairly linear rate over 60 seconds. The worst-case scenario is cooling opposite from the tabs, in which case the current continues to become more non-uniform throughout the 60 seconds, approaching a plateau of 14% at 60 seconds. For the adiabatic case, the system reaches a maximum non-uniformity at around 30 seconds and then starts to become more uniform again as the concentration and local state of charge effects begin to dominate the thermal effects. The case of cooling on the same side as the tabs performs in between the isothermal and adiabatic case, reaching a maximum non-uniformity at around 10 seconds. As can be seen, it is critical to consider the thermal effects in a battery as neglecting these effects can lead to significant inaccuracies in predicting local current distribution in the design or control of lithium-ion batteries.

3.2.3 Current Distribution Between Cells in a Stack

Thermal effects will also lead to non-uniform current distribution between cells in a planar stack. The above cell is simulated as part of a 20 cell stack and the current distribution between cells in the stack is calculated. The system assumes cooling with a heat transfer coefficient (h) of 0.01W/cm^2 K on the face of the end cells of the stack. The stack is treated as symmetric, so only half the stack is simulated; the first cell (at the stack center) transfers no heat on the side at the center of the stack. The average temperature in each cell over a 60 second discharge at 5C is shown in Figure 22. The ambient and initial stack temperature is 298K.

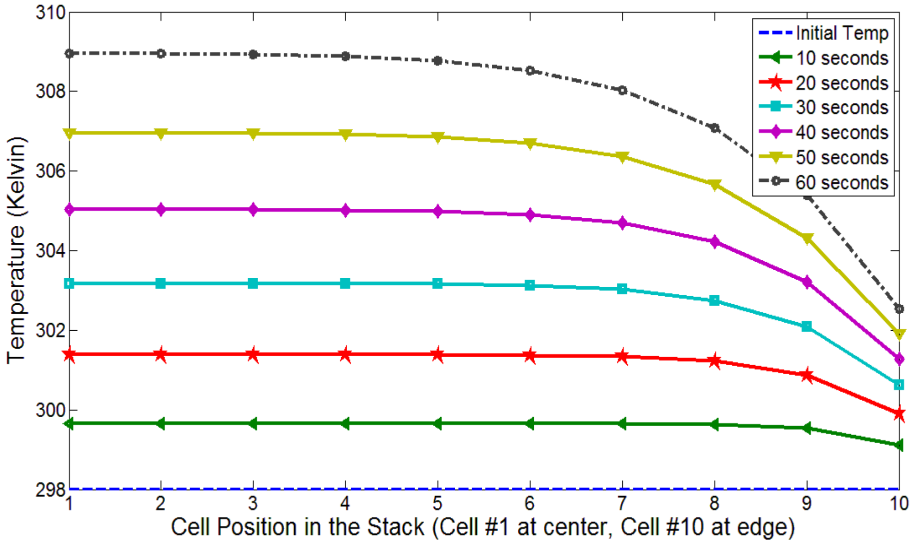

Figure 22: Average temperature in each cell over a 60 second discharge at 5C for a 20 cell stack (10 cells shown)

Over time, a steeper temperature gradient is generated from the end of the stack.

This temperature distribution will lead to increasing current non-uniformities between cells in the stack as seen in Figure 23, with less current going to the cooler cells towards the end of the stack. The current density shown is the overall average current density for each cell.

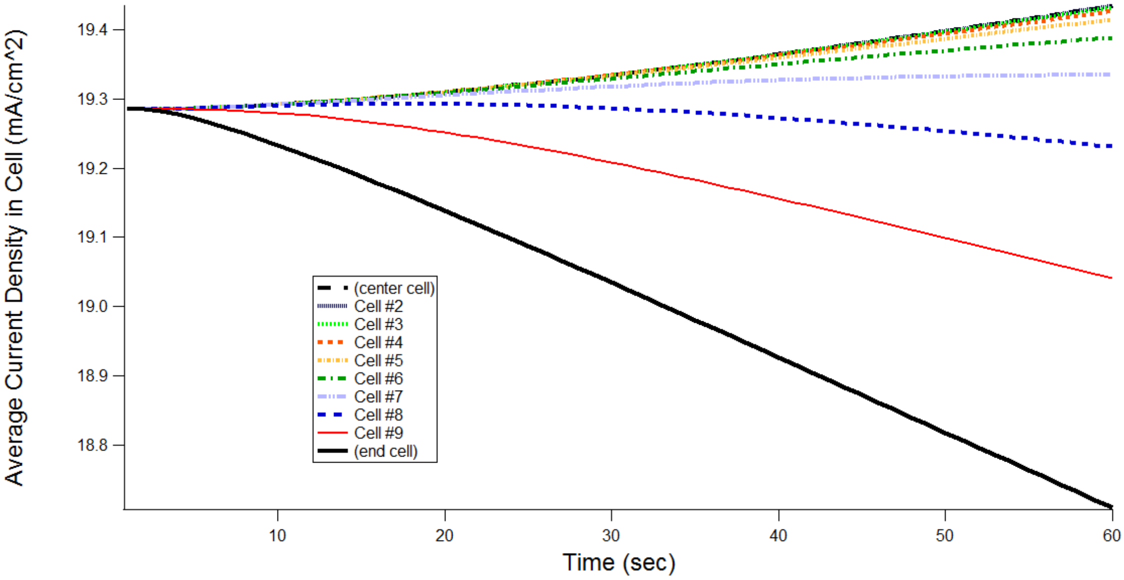

Figure 23: Average current density in each cell during a 60 second discharge at 5C in a 20 cell stack (10 cells shown).

3.3 DESIGN OPTIMIZATION OF CURRENT COLLECTOR THICKNESS AND TAB PLACEMENT

A significant portion of a battery cell is taken up by material that does not store energy including the separator, electrolyte, current collector foils, and casing. Based on a study by Johnson and White [35] in 2000 looking at commercialized lithium ion batteries approximately, 50% of the cell by volume and 60% by weight is taken up by these non-active materials. This indicates that there may be an opportunity to improve energy and power density by optimizing cell design. The current collector foils in their study on average took up 17% of the total mass of the battery and 7% of the volume. In portable electronic and vehicle battery applications, both volume and mass are at a premium so there is a strong incentive to minimize both size and weight in battery designs. One way to do this is to optimize the current collector thickness and current collector tab placement.

The following simulations investigating the influence of the current collector thickness and the current collector tab placement on battery behavior were run at an 80% initial state of charge. As in the prior examples, a 20x30cm battery cell with a single 4cm wide tab on each current collector foil is simulated. A more detailed listing of all of the material property data and design parameters are in Appendix A.

3.3.1 Impact of Current Collector Thickness on Battery Performance

The thickness of the current collector can have a significant impact on overall battery performance including efficiency, power and energy density, maximum power capabilities, heat generation rates, current and potential uniformity, and power losses.

As would be expected, as the current collector thickness increases the power output increases. This can be seen in Figure 24 for a cell discharged at an 8C rate (1C corresponds to a full discharge in 1 hour so 8C is a full discharge in 7.5 minutes). The increasing power output is primarily due to lower ohmic losses (I^2R) in the current collector foils due to the higher conductivity of thicker foils. To a much lesser extent the current uniformity can impact the overall power output due to electrochemical efficiencies, but in the cell simulated here the impact is <1%. The tab configuration is the same as in section 3.2 with tabs one quarter of the way in from either side along the 20cm edge of the battery.

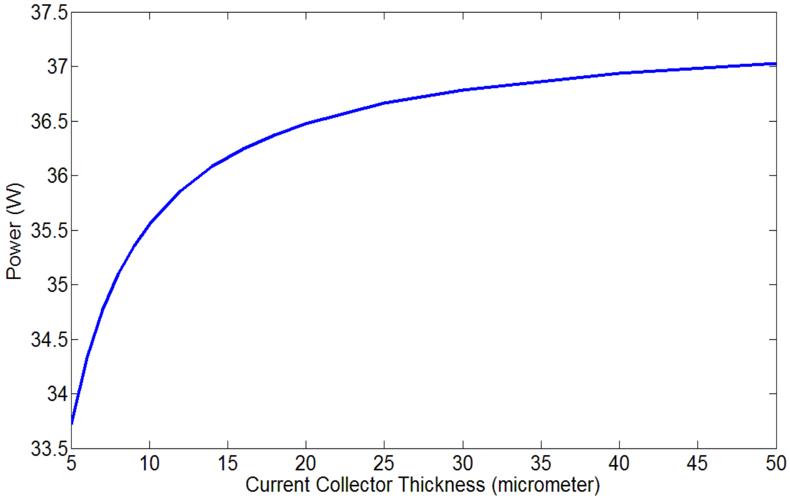

Figure 24: Overall cell power output versus current collector thickness

By dividing the total power output of the battery by the total volume of the battery cell, an overall power density can be obtained as seen in Figure 25. The total power continues to increase as the foil thickness increases, but so does the overall volume and mass of the battery, resulting in a maximum volumetric power density at 10µm for this particular cell discharged at an 8C rate. It should be noted that the foil thickness to maximize volumetric power density will be highly dependent on the size of the battery as well as the discharge rate.

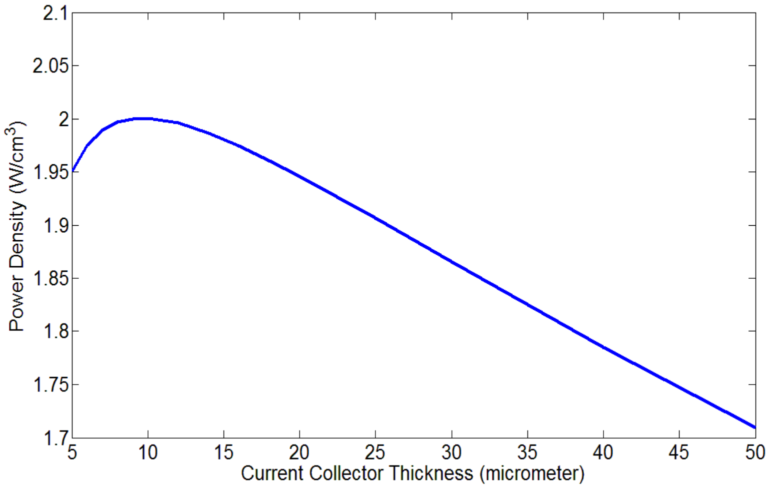

Figure 25: Volumetric power density versus current collector thickness

Power is calculated as total cell voltage at the tabs multiplied by the total cell current measured at the tabs. This is taken to be the instantaneous power at the start of discharge, so temperature effects and concentration gradients are not part of these results. Power density is calculated by taking the total cell power divided by the total cell volume, which includes the five layers (electrodes, separator, and foils) but not any casing or tab material. The current collector foil thickness is the total thickness in a battery stack configuration, where the foil would be shared by two electrodes. The listed thickness is for the aluminum current collector foil and the copper foil is chosen so that the conductivity is equal to the aluminum foil electrical conductivity at 298K.

Another important factor in the design of the current collector foils is the overall current uniformity of the system. As was seen in section 3.2, there will be some non-uniformities in the current distribution across the cell, with higher current densities occurring near the tabs. The current uniformity is quantified by dividing the maximum local current density by the minimum local current density as measured by the current entering a 1D electrochemical numerical node. Figure 26 shows how the current collector thickness influences the current uniformity of the system. For a 5µm foil the maximum current is 15% higher than the minimum at the start of discharge and this drops to less than 2% as the thickness is increased to 50µm.

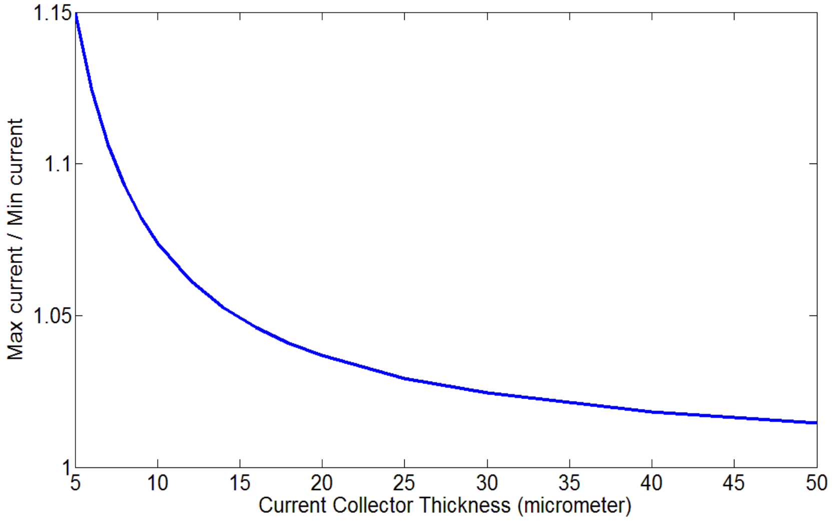

Figure 26: Maximum local current density divided by minimum local current density as a function of current collector thickness

3.3.2 Current Collector Thickness and Discharge Rate

The impact of current collector thickness on power losses, current non-uniformity and power density is investigated at current collector thicknesses between 5 and 50µm and discharge rates from 2-10C. In these examples, the tabs are located in the middle of the opposite 20cm edges (configuration D in Figure 29)

Figure 27 shows the percentage power loss in the current collector foils based on the current collector foil thickness and discharge rate. This is calculated by comparing the total power generated electrochemically in the battery to the measured power at the tabs.

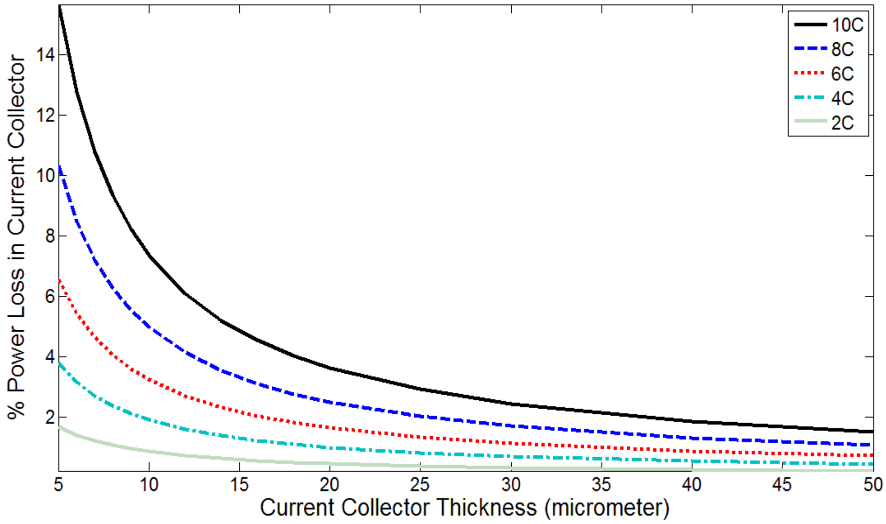

Figure 27: Percentage of the total electrochemical power generated that is lost in the current collector foils as a function of discharge rate and foil thickness

As expected, power losses (I^2R) in the current collector foil increases significantly with increasing discharge rate and decreasing current collector thickness. The higher the discharge rate, the more important it is to have thicker foils to minimize these power losses as well as to minimize the corresponding ohmic heating in the foils, which can lead to overheating and damage the battery. The current collector thickness to maximize overall volumetric power density also increases slightly with discharge rate as shown in Figure 28.

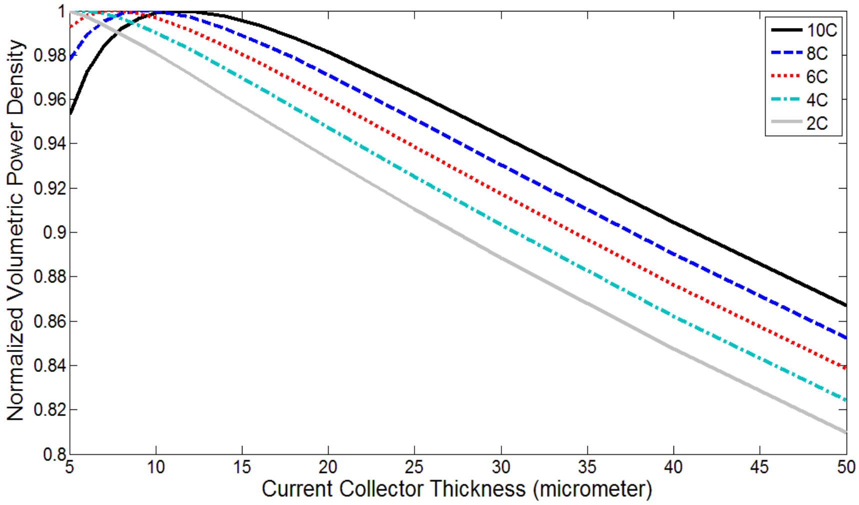

Figure 28: Normalized volumetric power density for various discharge rates as a function of current collector thickness. Power is normalized to the maximum power at each discharge rate.

In addition to maximizing the volumetric power density, other factors need to be taken into account in determining the optimal current collector thickness including the power losses, heat generation, and current non-uniformity effects of different current collector foil thickness.

3.3.3 Current Collector Tab Placement

The current collector tab placement in the system can also have a significant impact on overall battery performance. The tabs connect the current collector foils to the external circuit so all of the current flows through the tabs. Eight different tab configurations, shown in Figure 29, are compared.

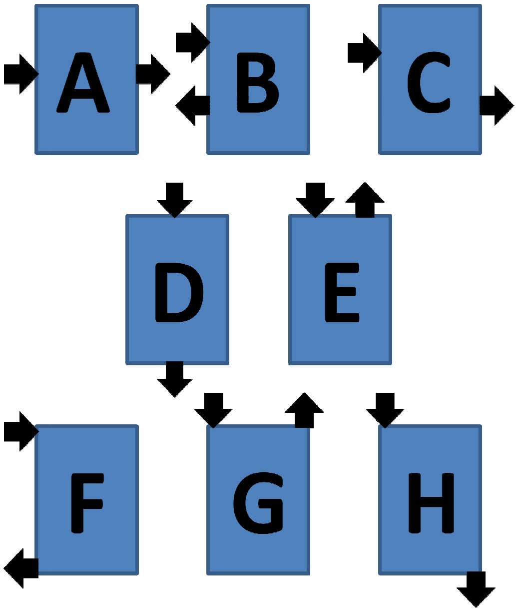

Figure 29: Tab configurations. Each black arrow represents a 4cm wide current collector tab. Arrows pointing towards the battery are anode current collector tabs and arrows pointing away are cathode current collector tabs.

Figure 30 shows the overall power density based on current collector tab placement. The lines are ordered from A-H in the order of decreasing power density. Configuration A, which has current collector tabs located in the middle of the long side of the battery exhibits the best overall power density as the average path length travelled by the current is minimized by this tab location. Configurations B and C are slightly worse and exhibit nearly identical power density performance. Configurations D and E, which have tabs located on the short side of the battery perform slightly worse than when tabs are located on the long edge. The worst performing tab configurations are when the tabs are located at the corners of the battery as shown with configurations F, G, and H. These three configurations exhibit nearly identical poor power density performance.

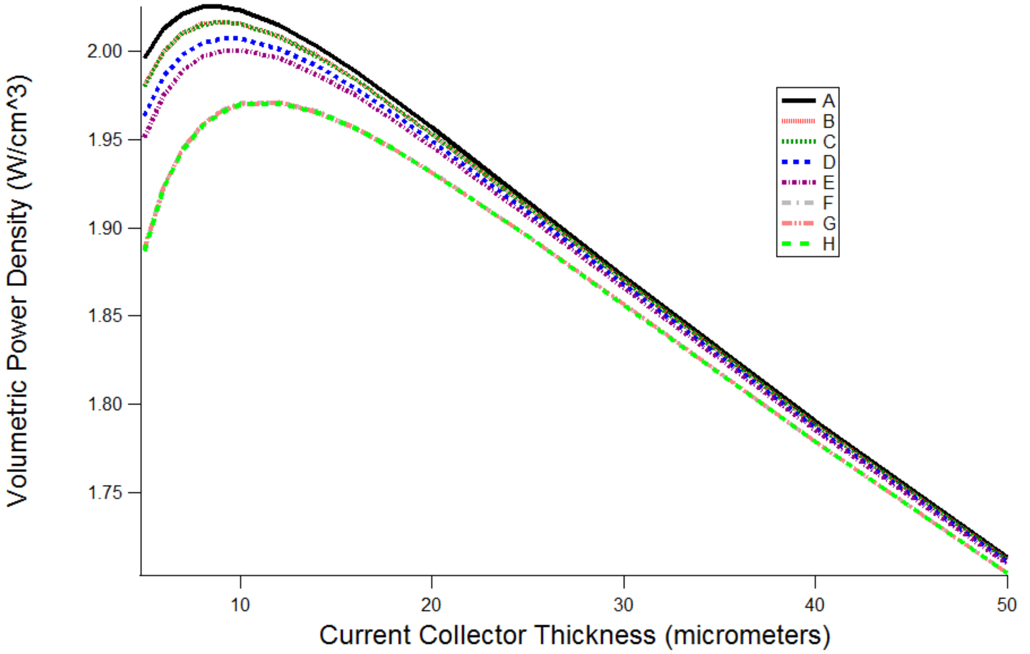

Figure 30: Volumetric power density based on current collector tab placement and current collector thickness. (See Figure 29 for tab configurations)

The eight tab positions are also compared for current uniformity in the plane of the separator as seen in Figure 31. From most uniform current to least uniform, the current the current collector tab positions are ordered as follows A, D, C, B, H, F, E, G. A more even current distribution leads to more uniform battery utilization and in general would be more desirable for a battery design. Configuration A has the best performance for both power density and current uniformity, but for the other tab configurations, better current uniformity does not necessarily translate into better overall power density. Configurations E and G, which have both tabs along the same short edge, exhibit the most non-uniform current density distribution. As would be expected, the differences in current uniformity are more substantial as the current collector gets thinner. When the current collector is thicker, the conductivity increases, and the voltage drop along the length of the foil is reduced.

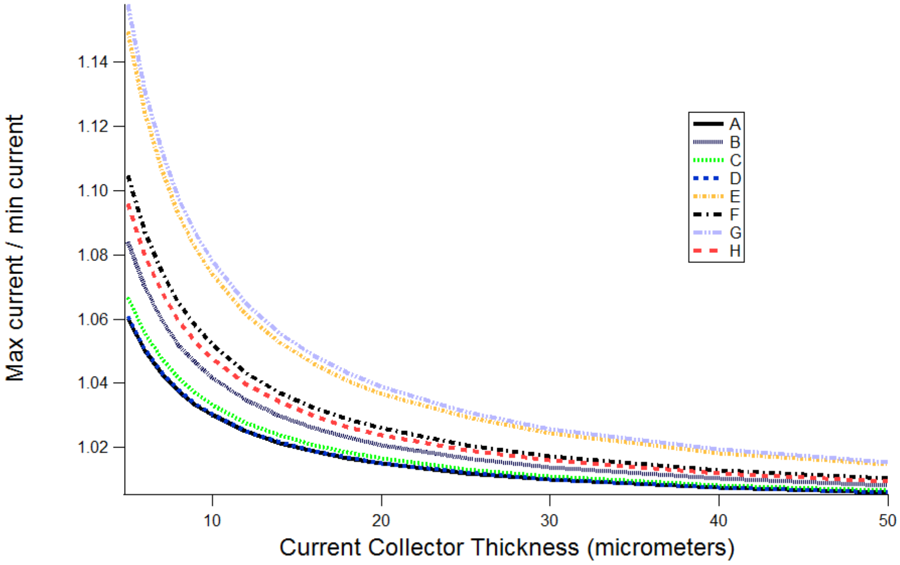

Figure 31: Maximum local current density divided by minimum local current density as a function of current collector thickness for different current collector tab configurations. (See Figure 29 for tab configurations)

3.3.4 Current Collector Tab Width

The width of the current collector tabs (taken to be 4cm in all the prior examples) will also influence current uniformity and power losses in the current collector foils. Figure 32 and Figure 33 below show the impact of current collector tab width on power losses and current uniformity. In these results, the tabs are located at the center of opposite long edges of the battery (configuration A in Figure 29). In the design of batteries, the width of the tabs needs to be balanced with the current collector thickness to arrive at an overall optimal design. A thicker tab will allow a more uniform current distribution and lower power losses with a thinner current collector foil. For example, a cell with 10cm wide tabs and a 5µm current collector foil will have the same power losses in the foil as a cell with a 4cm wide tab and a 20µm thick current collector foil. The trade-off between tab width and current collector thickness will depend on other overall design and space constraints for the battery.

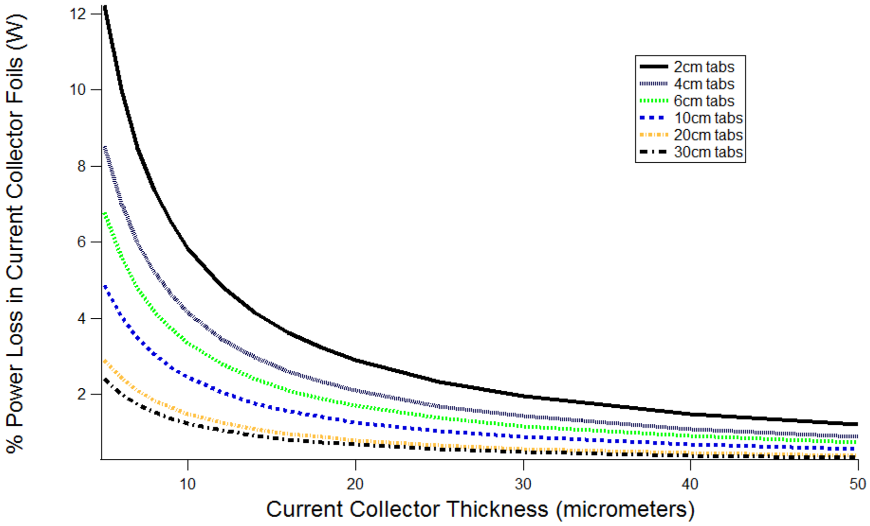

Figure 32: % Power loss in current collector foil as a function of current collector thickness and current collector tab width.

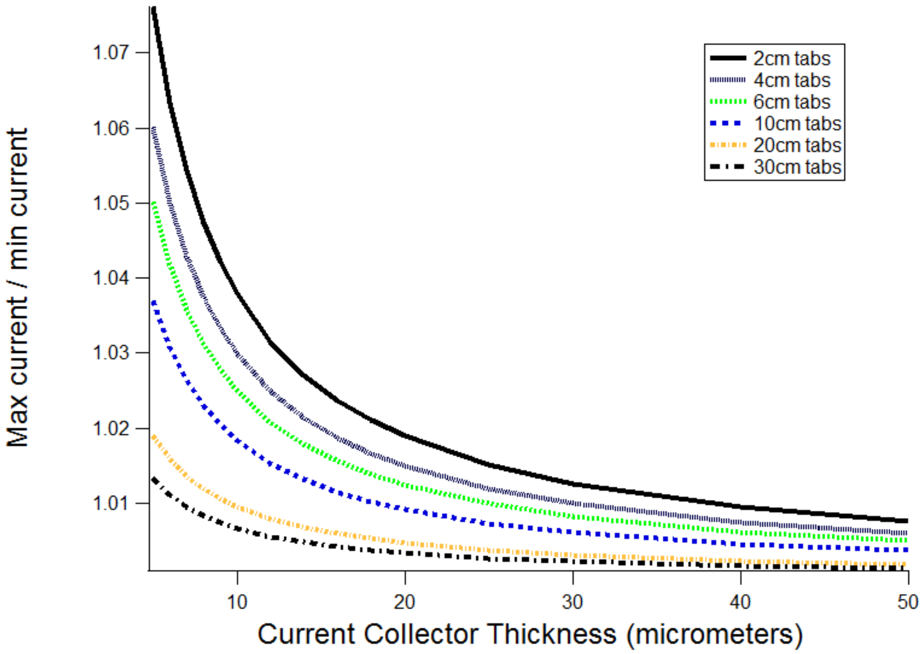

Figure 33: Maximum current divided by minimum current as a function of current collector thickness and current collector tab width.

3.4 LITHIUM PLATING

Lithium plating is a major concern with lithium ion batteries due to its impact on safety and long term durability. Lithium plating occurs when the local potential difference between the electrode and electrolyte ($\Phi_1 - \Phi_2$) drops below zero. The potential of the electrolyte is taken to be that of a hypothetical lithium reference electrode that can probe the solution immediately adjacent to the surface. If the reference electrode is taken to be reversible to lithium metal plating, this means that potentials more positive than the reference value would induce lithium metal dissolution, and potentials more negative than that reference would induce lithium plating on the electrode. The process of lithium plating results from current levels that are too high, or situations where the graphite anode becomes locally saturated with lithium.

In a hybrid electric vehicle, energy is recaptured during braking by charging the battery. This regenerative braking is often limited by the maximum safe power levels that the battery can accept based state of charge, temperature, and other factors that influence lithium plating risk. The higher the power levels that the battery can accept during a braking event the more fuel the vehicle can conserve. One of the major limitations on charging levels is lithium plating on the anode.

As was seen in section 3.2, there can be significant non-uniformities in current distribution along the length of the battery cell. Utilizing the cell average current density to predict lithium plating can result in under predicting the lithium plating risk. Also, as will be shown, the prior condition of the battery at the start of charging can influence the lithium plating risk, and should be taken into account in the design and control of batteries. By understanding these factors, vehicle fuel efficiency performance can be maximized while ensuring safe battery operation.

Figure 34 shows the minimum local electrode minus electrolyte potential ($\Phi_1 - \Phi_2$) in each 1D electrochemical numerical node in the battery during charging at a 1.25C rate. When this value drops below zero, lithium plating can occur. This is indicated by the regions in black on the figures. The same battery cell is simulated here as in Section 3.2. After 5 seconds of charging, lithium plating occurs at the edge of the battery just at the tabs. After 10 seconds of charging lithium plating occurs along the first 3cm of length of the battery. It is not until more than 15 seconds of charging that plating begins to occur in the center of the battery, which is close to the average overall current density. Taking a 1D approximation of the battery would falsely predict more than an additional 10 seconds of safe charging before lithium plating. This illustrates the importance of simulating the battery in three dimensions.

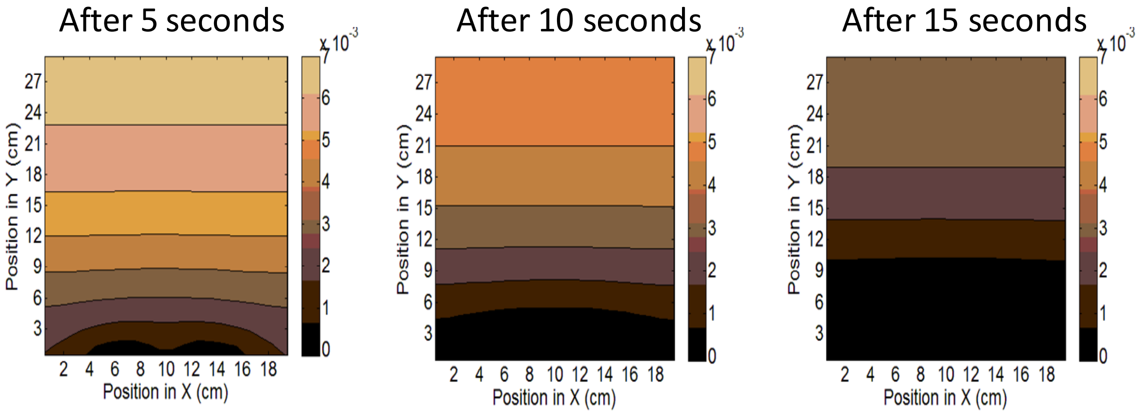

Figure 34: Minimum electrode potential minus electrolyte potential at each 1D electrochemical numerical node in the battery. Black region ($\Phi_1 - \Phi_2 <= 0$) denotes areas where lithium can plate.

The lowest ($\Phi_1 - \Phi_2$) values occur at the anode-separator interface as shown in Figure 35, as this is where reaction rates are highest. Based on these results, plating will preferentially occur at the anode-separator interface near the tabs.

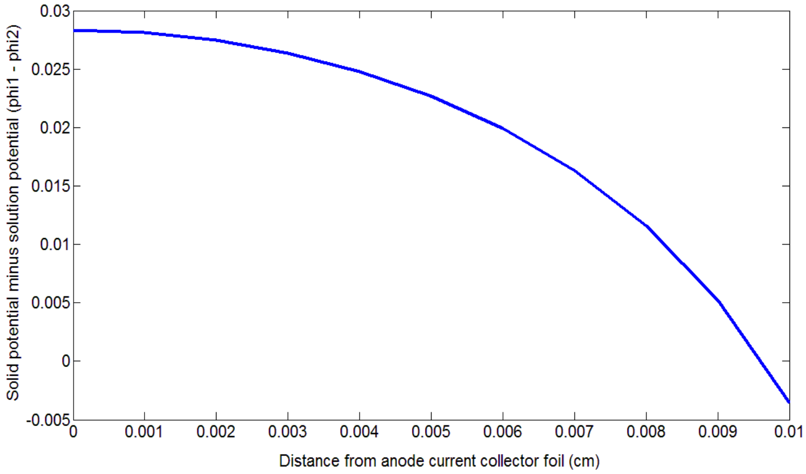

Figure 35: Solid potential minus solution potential (Φ1-Φ2) versus position in the anode for one of the 1D electrochemical nodes located at the current collector tab after 15 seconds of charging.

It is also important to take into account the prior condition of the battery in predicting lithium plating. The above case assumes the system starts at a uniform initial condition (x = 0.7 in Li_xC_6 everywhere in the anode) and also assumes that the entire battery is at the ambient temperature of 298K. Charging at 1.25C following a high discharge event, for example braking soon after a hard acceleration event, will result in a different potential profile in the battery.

An example is simulated where the battery is discharged adiabatically for 10 seconds at 5C followed by 30 seconds of charging at 1.25C. The state of charge of the overall battery at the start of the charging event is the same as in the previous example (x = 0.7 in Li_xC_6). The discharge event leads to both non-uniformities in temperature and concentration, which will influence the current and potential distribution in the battery at the start of charging. In the first example, when starting with uniform initial conditions, the maximum local current density in the battery is 9% above the minimum local current density, whereas when the charging event is preceded by the 5C discharge the maximum local current density is 13.2% above the minimum local current density.

Despite the more non-uniform current on charging, the minimum electrode potential minus electrolyte potential ($\Phi_1 - \Phi_2$) actually remains higher throughout the battery, making the lithium plating risk lower. During the discharge event, the reaction preferentially occurs at the electrode-separator interface as shown in Figure 36, resulting in a local lithium concentration lower than the x = 0.7 average throughout the anode as seen in Figure 37. This anode-separator interface will also be where the highest rate of reaction occurs on charging and the lower local lithium concentration in the anode here reduces the plating risk. As a result, even after 30 seconds of charging at a 1.25C rate, no lithium plating will occur anywhere in the battery.

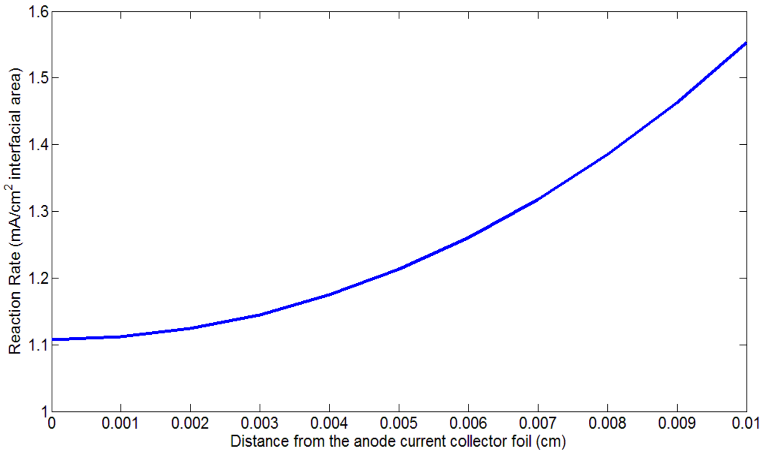

Figure 36: Reaction versus position in the anode

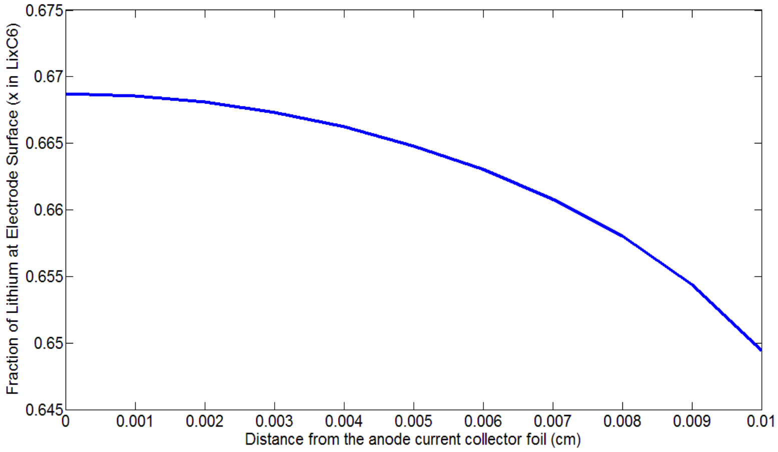

Figure 37: Lithium fraction at the electrode surface versus position in the anode

In a similar manner, prolonged charging events increase the risk of lithium plating as the concentration at the electrode surface at the anode-separator interface will increase more rapidly than the average concentration in the electrode due to the higher rates of reaction here. The changing concentration of lithium at the electrode surface across the thickness of the anode during a 1.25C charging is shown in Figure 38.

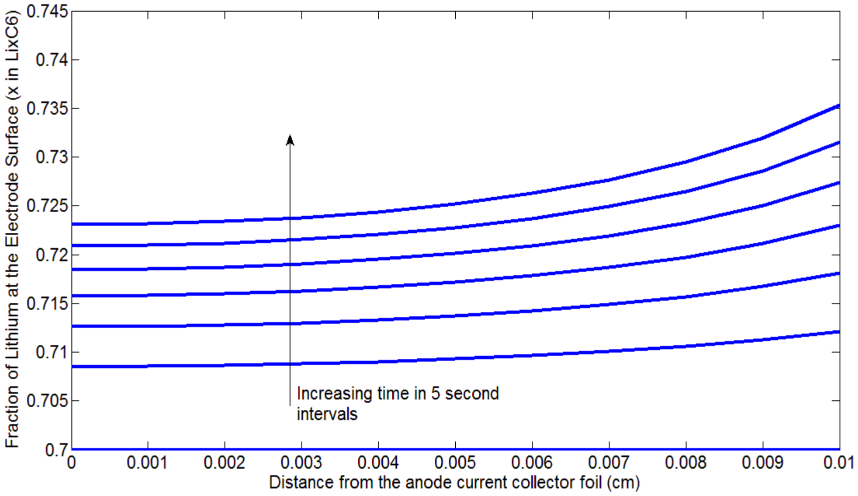

Figure 38: Lithium fraction at the electrode surface versus anode position over time

Taking into account the state of the battery at the start of charging event, beyond just the average state of charge of the battery, is important in determining safe charging levels. Prolonged periods of charging pose the highest risk, whereas charging events immediately preceded by a discharge are at a lower risk due to the lower concentrations of lithium at the anode-separator interface. It is also important to take into account the overall current distribution in the system in three dimensions to ensure that no portion of the battery is at risk for an overcharge condition.

3.5 OTHER MODEL USES

Beyond the examples shown here, the 3D thermal-electrochemical battery model can be used for a number of other applications for the design and control of batteries. Other parameters can be investigated for design optimization including macroscopic dimensions such as layer thicknesses, number of cell layers, battery width and height, or on the smaller scale: porosity and particle size effects. The model can also aid in the design of overall battery control systems to determine safe charge and discharge power levels under a variety of conditions. The thermal-electrochemical coupling can aid in the design of cooling systems and enhance understanding of how cooling system operation will influence battery behavior in three dimensions. The existing model can simulate single battery cells and prismatic cell stacks and is in the process of being expanded to spirally wound battery cells, which pose their own set of design and control challenges for large scale operation.

Developing large scale batteries for hybrid and electric vehicle applications poses a number of unique challenges including stricter standards on safety and long term durability, more significant thermal challenges due to both higher power loads and a wider range of ambient operating temperatures, greater non-uniformities in three dimensions, and greater cost pressures in order to be competitive with non-electrified vehicles. This development process can be aided with the development of improved computational models, such as this one, that can focus development efforts and minimize costly experimental iterations.

Appendix A: Material Property Data

The full set of material property data and design parameters used in the simulations are listed below. They come from a variety of sources in the literature as noted. Where applicable when the data is available, the properties are provided as a function of temperature and concentration.

A.1 ELECTROLYTE MATERIAL PROPERTIES

Property	**Value**	**Reference**
$\left(1-\frac{dlnc_o}{dlnc}\right)$	1	Assumed to be approximately constant
Initial concentration (moles/cm^3)	.001	Design parameter
Li$^+$ Transference number	0.4	[36]

Electrolyte Conductivity

$$\kappa = C(-10.5 + 0.0740T - 6.96\times10^{-5}T^2 + 0.668C - 0.0178CT + 2.8\times10^{-5}CT^2 + 0.494C^2 - 8.86\times10^{-4}C^2T)^2$$

[T is temperature in Kelvin; C is lithium ion concentration in Molarity] from [36]

(when C > 4.5 M C is set to equal 4.5M)

Thermodynamic Factor

$$\left(1+\frac{dlnf}{dlnc}\right) = \frac{(0.601 - 0.24C^{0.5} + 0.982\big(1 - 0.0052(T-298)\big)C^{1.5}}{(1-t_+)}$$

[C is lithium ion concentration in Molarity] Equation from [36]

Li$^+$ diffusion coefficient

$$D = 10^\wedge\left(-0.22c - 4.43 - \frac{54}{T-229+5C}\right)$$

[T is temperature in Kelvin; C is lithium ion concentration in Molarity] from [36]

A.2 ELECTRODE MATERIAL PROPERTIES:

Property	**LiC6**	**Reference**	**LiFePO4**	**Reference**
Diffusion Coefficient (cm^2/s)	9e-10	[37]	8e-14	[33]
% by volume of non-active additive	12%	Calculated from [38]	30%	Calculated from [38]
Max lithium concentration in active electrode ($moles/cm^3$)	.0287	Calculated (assuming LiC6 density of 2.27 g/cm^3 from [38])	0.0228	Calculated (assuming LiFePO4 density of 3.6 g/cm^3 from [38]
Particle Radius (cm)	11e-3	[38]	52e-6	[38]
Porosity	0.4	Design Parameter	0.4	Design Parameter
Active Interfacial Area Per Unit Volume	1.64e3	Calculated from $a = \frac{3\varepsilon}{r}$	3.46e5	Calculated from $a = \frac{3\varepsilon}{r}$
SEI Layer Resistance ($Ohms/cm^2$)	230	[38]	0	
Electrical Conductivity (S/cm)	1	[39]	5e-3	[33]
Butler-Volmer (α)	0.5	[26]	0.5	[26]

Exchange Current Density

$$i_o = i_{o,ref}\left(\frac{c}{c_{ref}}\right)^{0.5}\left(\frac{cs}{cs_{ref}}\right)^{0.5}$$

Equation from [24], where c_{ref} the Li^+ reference concentration is taken to be the initial electrolyte concentration of 1M, and cs_{ref} is taken to be the lithium concentration in each electrode at 50% SOC.

Lithium Graphite:

$$i_{o,ref} = 20e^{(-30000/8.314T)}$$

Equation derived from [40]

[T is temperature in Kelvin]

Lithium Iron Phosphate:

$$i_{o,ref} = (1.34 \times 10^{-3})e^{(-15000/8.314T)}$$

Equation estimated from data in [41] and [42]

[T is temperature in Kelvin]

Lithium Graphite Entropy:

$$\frac{dU}{dT} = 344.1347148 \times \frac{\exp\left(-32.9633287x + 8.316711484\right)}{1 + 749.0756003 \times \exp(-34.7909964 + 8.887143624)} - 0.8520278805x + 0.36229929x^2 + 0.2698001697$$

Equation from [43], where x is fraction of lithium in Li_xC_6

Lithium Iron Phosphate Entropy:

$$\frac{dU}{dT} = -0.35376x^8 + 1.3902x^7 - 2.2585x^6 + 1.9635x^5 - 0.98716x^4 + 0.28857x^3 - 0.046272x^2 + 0.0032158x - 1.9186 \times 10^{-5}$$

Curve fit to data from [44], where x is fraction of lithium in Li_xFePO4

Open Circuit Potential

$$U = U_{ref} + \left(T - T_{ref}\right)\frac{dU}{dT}$$

Lithium Graphite:

For x > 0.95

$$U_{ref} = -162.54x^3 + 449.21x^2 - 413.89x + 127.22$$

For 0.90 < x < 0.95

$$U_{ref} = \frac{(-162.54x^3 + 449.21x^2 - 413.89x + 127.22)}{2} + \frac{(-1.6525x^4 + 3.6877x^3 - 2.7892x^2 + 0.7551x + 0.0629)}{2}$$

For 0.2032 < x < 0.9

$$U_{ref} = -1.6525x^4 + 3.6877x^3 - 2.7892x^2 + 0.7551x + 0.0629$$

For x < 0.2032

$$U_{ref} = 1683.3x^4 - 1148.7x^3 + 286.93x^2 - 31.745x + 1.5005$$

Equation developed by curve fitting to experimental data in [45] where x is the fraction of lithium in Li_xC_6.

Lithium Iron Phosphate

For x < 0.048

$$U_{ref} = 3.02 \times 10^5 x^4 - 4.34 \times 10^3 x^3 + 2.46 \times 10^3 x^2 - 69.7x + 4.3$$

For 0.048 < x <0.892

$$U_{ref} = 3.42$$

For x > 0.892

$$U_{ref} = -5.76 \times 10^3 x^4 + 2.07 \times 10^4 x^3 - 2.79 \times 10^4 x^2 + 1.67 \times 10^4 x - 3.77 \times 10^3$$

Equation derived from experimental data in [46], where x is fraction of Lithium in Li_xFePO_4

A.3 THERMAL PROPERTY DATA

Material	**Volumetric Specific Heat (J/cm^3 K)**	**Reference**
Copper	3.44	[47]
Lithium Graphite	1.9	[7]
Separator	2	[7]
LiFePO4	2	Estimate (data unavailable)
Aluminum	2.42	[47]

Material	**Thermal Conductivity (W/cm K)**	**Reference**
Copper	4.01	[47]
Lithium Graphite	.01	[7]
Separator	.005	[7]
LiFePO4	.01	Estimate (data unavailable)
Aluminum	2.37	[47]

A.4 CURRENT COLLECTOR FOIL DATA

Copper Current Collector Electrical Conductivity:

$$\sigma_{Cu} = -0.04889T^3 + 54.65T^2 - 21800T + 3.52 \times 10^6$$

Curve fit to data from [47] in S/cm for [200 < T < 400 K]

Aluminum Current Collector Electrical Conductivity

$$\sigma_{Al} = -0.0325T^3 + 37.07T^2 - 15000T + 2.408 \times 10^6$$

Curve fit to data from [47] in S/cm for [200 < T < 400 K]

A.5 DESIGN PARAMETERS

Cell Layer	**Thickness (cm)**
Anode	1e-2 (5.5e-3 for 3.1)
Cathode	1.5e-2 (8.5e-3 for 3.1)
Separator	3e-3

Battery Height (cm)	30
Battery Width (cm)	20

Appendix B: Discretization Error Check

The number of mesh spaces within the 1D electrochemical model, the number of 1D electrochemical nodes, and the number of time steps were varied for an adiabatic 5C discharge over 20 seconds to estimate the error associated with the parameters chosen for this thesis. The number of time steps were varied from 5-40, the number of mesh spaces in each electrode varied from 5-20, and the number of 1D electrochemical nodes varied from 24 to 1350 in configurations of 4x6, 5x8, 10x15, 20x30, and 30x45.

The figures below show the error percentage associated with the max local current density and temperature when independently varying the number of time steps, mesh spaces, and electrochemical nodes. The error % is calculated from the following equation:

$$error\ \% = \frac{X_n - X_{max}}{X_{max}} \times 100$$

Where X is the parameter being measured (i.e. max current density or max local temperature) calculated at either the maximum number of mesh spaces, time steps, or electrochemical nodes simulated (for X_{max}) or some lower value of these parameters (for X_n). The number of mesh spaces, time steps, and electrochemical nodes used in the simulations for this thesis are circled on each of the plots.

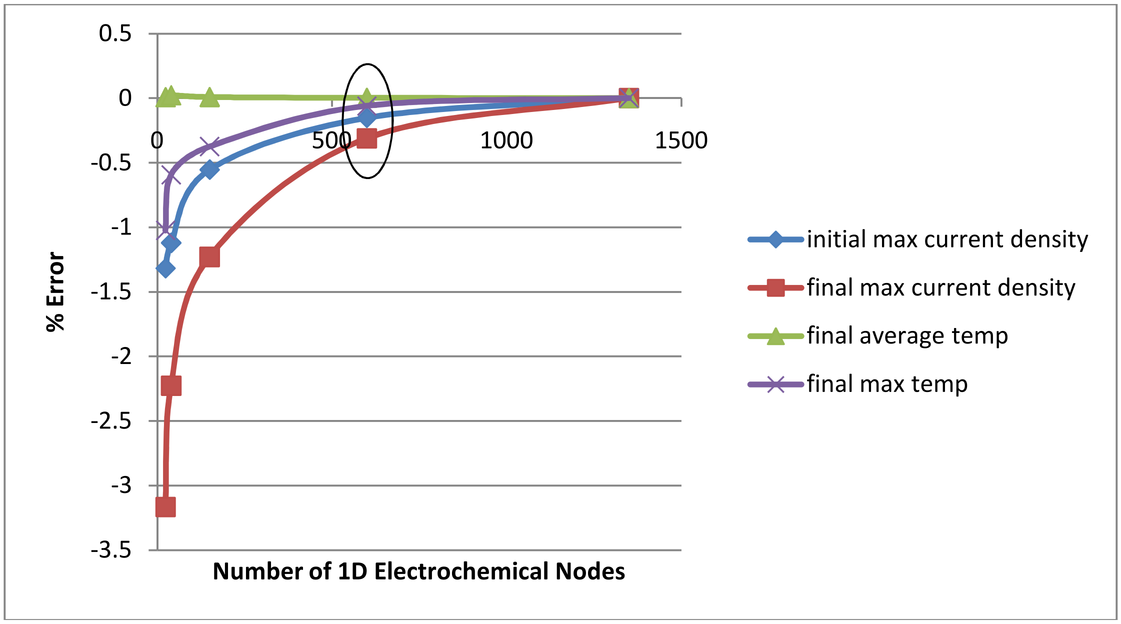

Figure 39: Error associated with varying the number of 1D electrochemical nodes

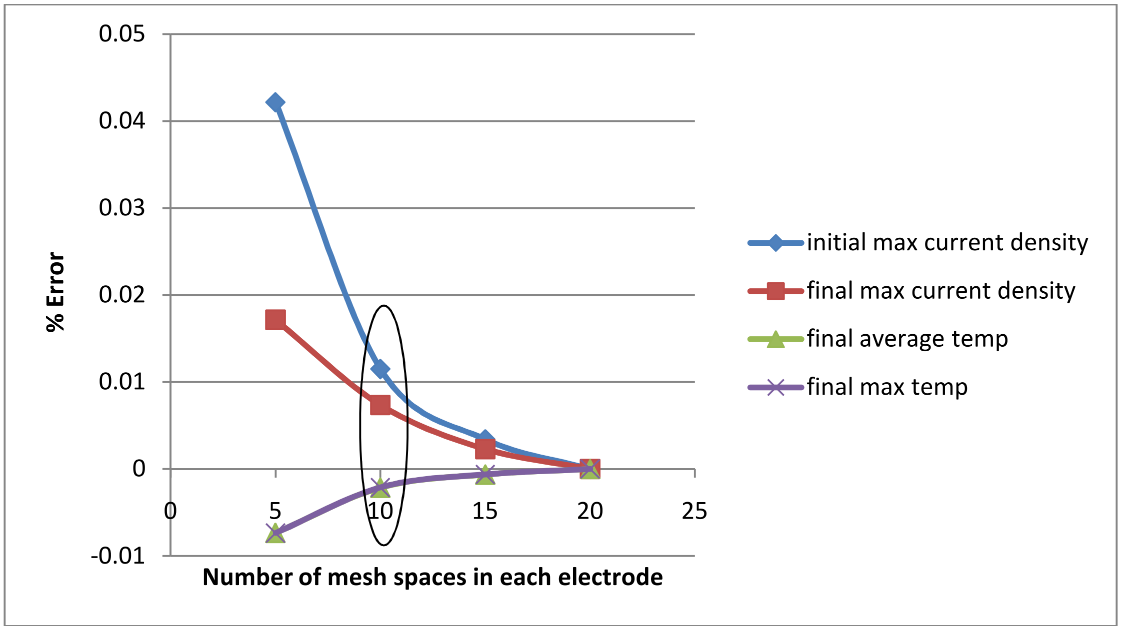

Figure 40: Error associated with varying the number of mesh spaces in each electrode

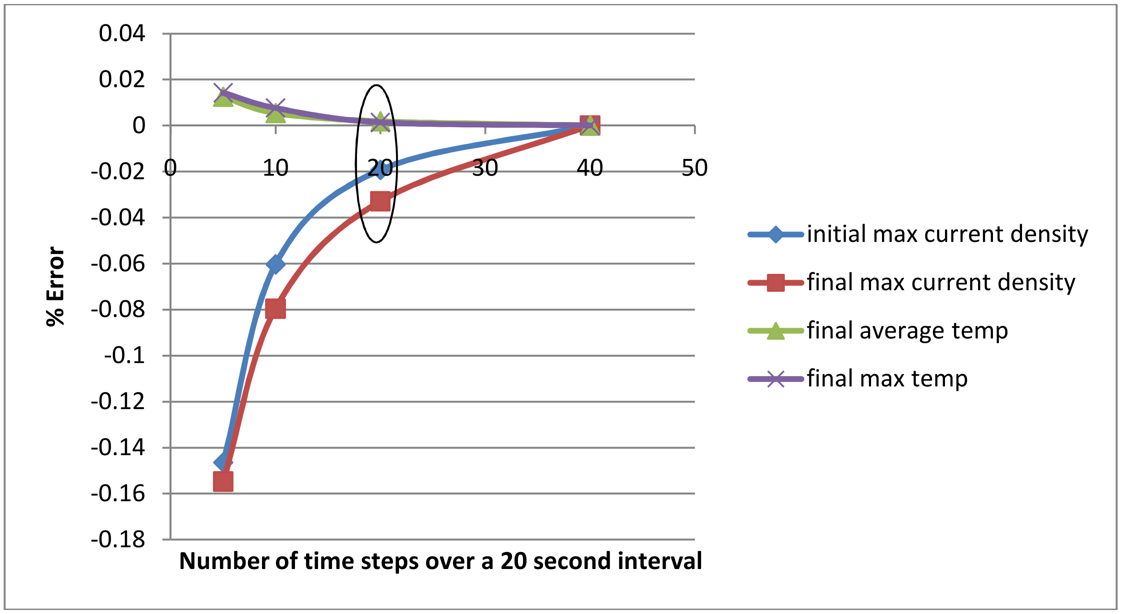

Figure 41: Error associated with varying the number of time steps over a 20 second interval

Work Cited

[1] J. Newman and W. Tiedemann, “Temperature Rise in a Battery Module with Constant Heat Generation,” *Journal of The Electrochemical Society*, vol. 142, Apr. 1995, pp. 1054-1057.

[2] Y. Chen and J.W. Evans, “Heat Transfer Phenomena in Lithium/Polymer-Electrolyte Batteries for Electric Vehicle Application,” *Journal of The Electrochemical Society*, vol. 140, Jul. 1993, pp. 1833-1838.

[3] Y. Chen and J.W. Evans, “Three-Dimensional Thermal Modeling of Lithium-Polymer Batteries under Galvanostatic Discharge and Dynamic Power Profile,” *Journal of The Electrochemical Society*, vol. 141, Nov. 1994, pp. 2947-2955.

[4] S. Al Hallaj, H. Maleki, J.S. Hong, and J.R. Selman, “Thermal modeling and design considerations of lithium-ion batteries,” *Journal of Power Sources*, vol. 83, Oct. 1999, pp. 1-8.

[5] C.R. Pals and J. Newman, “Thermal Modeling of the Lithium/Polymer Battery,” *Journal of The Electrochemical Society*, vol. 142, Oct. 1995, pp. 3282-3288.

[6] L. Song and J.W. Evans, “Electrochemical-Thermal Model of Lithium Polymer Batteries,” *Journal of The Electrochemical Society*, vol. 147, Jun. 2000, pp. 2086-2095.

[7] S. Chen, C. Wan, and Y. Wang, “Thermal analysis of lithium-ion batteries,” *Journal of Power Sources*, vol. 140, Jan. 2005, pp. 111-124.

[8] J. Lee, K.W. Choi, N.P. Yao, and C.C. Christianson, “Three-Dimensional Thermal Modeling of Electric Vehicle Batteries,” *Journal of The Electrochemical Society*, vol. 133, Jul. 1986, pp. 1286-1291.

[9] T.I. Evans and R.E. White, “A Thermal Analysis of a Spirally Wound Battery Using a Simple Mathematical Model,” *Journal of The Electrochemical Society*, vol. 136, 1989, pp. 2145-2152.

[10] D.M. Bernardi, H. Gu, and A.Y. Schoene, “Two-Dimensional Mathematical Model of a Lead-Acid Cell,” *Journal of The Electrochemical Society*, vol. 140, 1993, pp. 2250-2258.

[11] M. Tang, P. Albertus, and J. Newman, “Two-Dimensional Modeling of Lithium Deposition during Cell Charging,” *Journal of The Electrochemical Society*, vol. 156, May. 2009, pp. A390-A399.

[12] K.H. Kwon, C.B. Shin, T.H. Kang, and C. Kim, “A two-dimensional modeling of a lithium-polymer battery,” *Journal of Power Sources*, vol. 163, Dec. 2006, pp. 151-157.

[13] M.W. Verbrugge, “Three-dimensionai temperature and current distribution in a battery module,” *AIChE Journal*, vol. 41, 1995, pp. 1550-1562.

[14] D.R. Baker and M.W. Verbrugge, “Temperature and Current Distribution in Thin-Film Batteries,” *Journal of The Electrochemical Society*, vol. 146, Jul. 1999, pp. 2413-2424.

[15] J.N. Reimers, “Predicting current flow in spiral wound cell geometries,” *Journal of Power Sources*, vol. 158, Jul. 2006, pp. 663-672.

[16] J.N. Harb and R.M. LaFollette, “Mathematical Model of the Discharge Behavior of a Spirally Wound Lead-Acid Cell,” *Journal of The Electrochemical Society*, vol. 146, Mar. 1999, pp. 809-818.

[17] Gi-Heon Kim, Smith, Kandler, and Ahmad, Pesaran, “Three-Dimensional Electrochemical Thermal Coupled Model of Large Format Cylindrical Lithium Ion Cells,” Oct. 2007.

[18] Harb, John N, “The Influence of Current Distribution on Battery Design and Performance,” May. 2009.

[19] D. Bharathan, A. Pesaran, A. Vlahinos, and G. Kim, “Improving battery design with electro-thermal modeling,” *Vehicle Power and Propulsion, 2005 IEEE Conference*, 2005, p. 8 pp.

[20] Y. Inui, Y. Kobayashi, Y. Watanabe, Y. Watase, and Y. Kitamura, “Simulation of temperature distribution in cylindrical and prismatic lithium ion secondary batteries,” *Energy Conversion and Management*, vol. 48, Jul. 2007, pp. 2103-2109.

[21] K. Kumaresan, G. Sikha, and R.E. White, “Thermal Model for a Li-Ion Cell,” *Journal of The Electrochemical Society*, vol. 155, Feb. 2008, pp. A164-A171.

[22] C.R. Pals and J. Newman, “Thermal Modeling of the Lithium/Polymer Battery,” *Journal of The Electrochemical Society*, vol. 142, Oct. 1995, pp. 3274-3281.

[23] M. Doyle, T.F. Fuller, and J. Newman, “Modeling of Galvanostatic Charge and Discharge of the Lithium/Polymer/Insertion Cell,” *Journal of The Electrochemical Society*, vol. 140, Jun. 1993, pp. 1526-1533.

[24] K. Thomas, J. Newman, and R. Darling, “Mathematical Modeling of Lithium Batteries,” *Advances in Lithium-Ion Batteries*, 2002, pp. 345-392.

[25] K.K. Patel, J.M. Paulsen, and J. Desilvestro, “Numerical simulation of porous networks in relation to battery electrodes and separators,” *Journal of Power Sources*, vol. 122, Jul. 2003, pp. 144-152.

[26] J.S. Newman and K.E. Thomas-Alyea, *Electrochemical systems*, Wiley-IEEE, 2004.

[27] C.M. Doyle, *Design and simulation of lithium rechargeable batteries*, 1995.

[28] D. Bernardi, E. Pawlikowski, and J. Newman, “A General Energy Balance for Battery Systems,” *Journal of The Electrochemical Society*, vol. 132, Jan. 1985, pp. 5-12.

[29] L. Rao and J. Newman, “Heat-Generation Rate and General Energy Balance for Insertion Battery Systems,” *Journal of The Electrochemical Society*, vol. 144, 1997, pp. 2697-2704.

[30] K.E. Thomas and J. Newman, “Thermal Modeling of Porous Insertion Electrodes,” *Journal of The Electrochemical Society*, vol. 150, Feb. 2003, pp. A176-A192.

[31] W. Tiedemann and J. Newman, “Current and Potential Distributions in Lead-Acid Battery Plates,” *Proc. Symp. Battery Des. Optimization, The Electrochemical Society*, 1979, p. 1.

[32] J. Shim and K.A. Striebel, “Cycling performance of low-cost lithium ion batteries with natural graphite and LiFePO4,” *Journal of Power Sources*, vol. 119-121, Jun. 2003, pp. 955-958.

[33] V. Srinivasan and J. Newman, “Discharge Model for the Lithium Iron-Phosphate Electrode,” *Journal of The Electrochemical Society*, vol. 151, Oct. 2004, pp. A1517-A1529.

[34] K. Striebel, J. Shim, V. Srinivasan, and J. Newman, “Comparison of LiFePO[sub 4] from Different Sources,” *Journal of The Electrochemical Society*, vol. 152, Apr. 2005, pp. A664-A670.

[35] B.A. Johnson and R.E. White, “Characterization of commercially available lithium-ion batteries,” *Journal of Power Sources*, vol. 70, Jan. 1998, pp. 48-54.

[36] L.O. Valoen and J.N. Reimers, “Transport Properties of LiPF[sub 6]-Based Li-Ion Battery Electrolytes,” *Journal of The Electrochemical Society*, vol. 152, May. 2005, pp. A882-A891.

[37] S.G. Stewart, V. Srinivasan, and J. Newman, “Modeling the Performance of Lithium-Ion Batteries and Capacitors during Hybrid-Electric-Vehicle Operation,” *Journal of The Electrochemical Society*, vol. 155, 2008, pp. A664-A671.

[38] V. Srinivasan and J. Newman, “Design and Optimization of a Natural Graphite/Iron Phosphate Lithium-Ion Cell,” *Journal of The Electrochemical Society*, vol. 151, Oct. 2004, pp. A1530-A1538.

[39] M. Doyle and Y. Fuentes, “Computer Simulations of a Lithium-Ion Polymer Battery and Implications for Higher Capacity Next-Generation Battery Designs,” *Journal of The Electrochemical Society*, vol. 150, Jun. 2003, pp. A706-A713.

[40] S. Surampudi, E.S. Meeting, E.S.B. Division, and E.S.E.T. Division, *Lithium batteries*, The Electrochemical Society, 2000.

[41] U.S. Kasavajjula, C. Wang, and P.E. Arce, “Discharge Model for LiFePO[sub 4] Accounting for the Solid Solution Range,” *Journal of The Electrochemical Society*, vol. 155, Nov. 2008, pp. A866-A874.

[42] M. Takahashi, S. Tobishima, K. Takei, and Y. Sakurai, “Reaction behavior of LiFePO4 as a cathode material for rechargeable lithium batteries,” *Solid State Ionics*, vol. 148, Jun. 2002, pp. 283-289.

[43] V. Srinivasan and C.Y. Wang, “Analysis of Electrochemical and Thermal Behavior of Li-Ion Cells,” *Journal of The Electrochemical Society*, vol. 150, Jan. 2003, pp. A98-A106.

[44] J.L. Dodd, “Phase composition and dynamical studies of lithium iron phosphate,” May. 2007.

[45] M.W. Verbrugge and B.J. Koch, “Electrochemical Analysis of Lithiated Graphite Anodes,” *Journal of The Electrochemical Society*, vol. 150, Mar. 2003, pp. A374-A384.

[46] A. Yamada, H. Koizumi, S. Nishimura, N. Sonoyama, R. Kanno, M. Yonemura, T. Nakamura, and Y. Kobayashi, “Room-temperature miscibility gap in LixFePO4,” *Nat Mater*, vol. 5, May. 2006, pp. 357-360.

[47] *CRC Handbook of Chemistry and Physics*, Cleveland, Ohio: CRC Press, 1977.

Vita

Rachel Ellen Gerver was born on March 12, 1981 in Athens, Georgia to April Kihlstrom and Joseph Gerver. She grew up in Cherry Hill, NJ. Attending Stanford University as an undergrad, she received a BS in Mechanical Engineering in June 2004. While an undergraduate, she interned in R&D at Coapt Systems, a biomedical device company, and in the materials area at GM. She also worked as a research assistant in the human-computer interaction lab at Stanford University. An internship in the advanced portfolio planning group at GM Europe looking at long term corporate strategy for electrified vehicles, sparked her initial interest in batteries for automotive applications. After college, she worked at General Motors for three years, where she was responsible for managing the fuel economy and drive quality on several hybrid electric vehicle programs. While at the University of Texas at Austin, she worked as a teaching assistant for a materials processing lab for two semesters in addition to working as a research assistant in the Meyers research group doing computational modeling work on Li-ion batteries.

Permanent address: 3009 Dana St.
Apt. A
Berkeley, CA 94705

This thesis was typed by the author.